

AIRE relies on Z-DNA to flag gene targets for thymic T cell tolerization

<https://doi.org/10.1038/s41586-024-07169-7>

Yuan Fang^{1,2}, Kushagra Bansal³, Sara Mostafavi^{4,5}, Christophe Benoist¹ & Diane Mathis^{1✉}

Received: 14 February 2023

Accepted: 6 February 2024

Published online: 13 March 2024

 Check for updates

AIRE is an unconventional transcription factor that enhances the expression of thousands of genes in medullary thymic epithelial cells and promotes clonal deletion or phenotypic diversion of self-reactive T cells^{1–4}. The biological logic of AIRE's target specificity remains largely unclear as, in contrast to many transcription factors, it does not bind to a particular DNA sequence motif. Here we implemented two orthogonal approaches to investigate AIRE's *cis*-regulatory mechanisms: construction of a convolutional neural network and leveraging natural genetic variation through analysis of F1 hybrid mice⁵. Both approaches nominated Z-DNA and NFE2–MAF as putative positive influences on AIRE's target choices. Genome-wide mapping studies revealed that Z-DNA-forming and NFE2L2-binding motifs were positively associated with the inherent ability of a gene's promoter to generate DNA double-stranded breaks, and promoters showing strong double-stranded break generation were more likely to enter a poised state with accessible chromatin and already-assembled transcriptional machinery. Consequently, AIRE preferentially targets genes with poised promoters. We propose a model in which Z-DNA anchors the AIRE-mediated transcriptional program by enhancing double-stranded break generation and promoter poisoning. Beyond resolving a long-standing mechanistic conundrum, these findings suggest routes for manipulating T cell tolerance.

Deep learning has recently emerged as a powerful tool for uncovering complex genomic-sequence patterns that are predictive of various functional features in the genome⁶. Convolutional neural networks (CNNs)—a regularized type of feed-forward network—are some of the most established deep-learning algorithms, and have been successfully applied to the analysis of various types of genomic data with impressive results⁷. The ability of CNNs to model complex nonlinear dependencies between sequence features of arbitrary lengths makes them an attractive approach for investigating the *cis*-regulatory elements distinguishing AIRE-target genes.

Another powerful strategy for systematic exploration of *cis*-regulatory mechanisms is to exploit the natural genetic variation in target-gene *cis*-regulatory elements in different mouse strains. In particular, the F1-hybrid approach, which eliminates confounding influences of *trans* factors, has been used successfully in several immunological contexts^{5,8}. This approach seemed ideal for identifying DNA-sequence features underlying AIRE's target specificity by unbiasedly testing the association between genetic variation in each transcription factor (TF)-binding motif and allelic imbalances in the chromatin accessibility and expression of AIRE-induced genes.

Employing a CNN

To distinguish the extended-promoter sequences of previously collated sets of AIRE-induced and expression-matched AIRE-neutral genes⁹,

we built and trained a CNN model with dilated convolutional layers and residual skip connections⁷. This approach followed a relatively new paradigm in the deep-learning field: pre-training on large-scale datasets to acquire generic knowledge and then transfer the knowledge to specific downstream tasks, termed the fine-tuning process. At that point, inputs to the model were extended-promoter sequences from the C57BL/6J genome, that is, DNA stretches $\pm 1,024$ bp from the transcriptional start sites (TSSs); outputs were predictions as to whether the input sequence was from an AIRE-induced or AIRE-neutral gene. Our overall two-stage strategy and diverse quality-control data are depicted in Extended Data Fig. 1 and additional explanations are provided in the Supplementary Notes.

To retrieve relevant sequence features learned by the deep CNN, we computed a contribution score to the output prediction (gradient \times input) for each input nucleotide using back-propagation. We then extracted the stretch of input sequence with the highest positive contribution scores for each input DNA sequence, thereby highlighting the regions that are most predictive of AIRE-induced genes. These subsequences were scanned for both *de novo* motifs and known TF-binding motifs. (CA)_n repeats (Methods and Supplementary Notes) and the NFE2–MAF-binding motif (a specific type of bZIP-family TF-binding motif)¹⁰ were enriched in the regions with the largest positive gradients (Fig. 1a and Supplementary Table 1), as exemplified by the contribution-score profiles of four AIRE-induced genes (Extended Data Fig. 2a).

¹Department of Immunology, Harvard Medical School, Boston, MA, USA. ²Department of Molecular and Cellular Biology, Harvard University, Cambridge, MA, USA. ³Molecular Biology and Genetics Unit, Jawaharlal Nehru Centre for Advanced Scientific Research, Bangalore, India. ⁴Paul G. Allen School of Computer Science and Engineering, University of Washington, Seattle, WA, USA. ⁵Canadian Institute for Advanced Research, Toronto, Ontario, Canada. ✉e-mail: dm@hms.harvard.edu

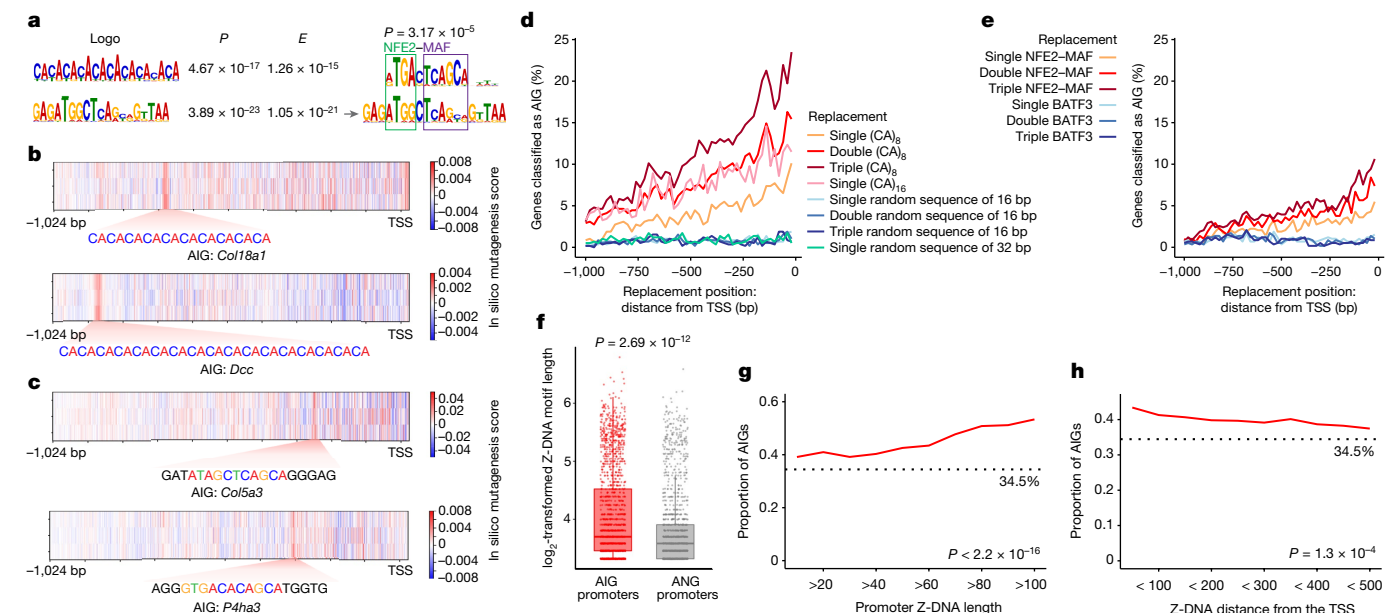


Fig. 1 | The Z-DNA and NFE2-MAF-binding motifs are salient features of the extended promoters of AIRE-induced genes. **a**, Motifs enriched in the regions with the largest positive contribution scores. **b, c**, The ISM scores for promoters of two AIRE-induced genes containing (CA)_n repeats (**b**) or NFE2-MAF-binding motifs (**c**). Each of the three rows shows results for one possible substitution in the order of A to C to G to T from top to bottom. Decreased (red) and increased (blue) predictive probability as an AIRE-induced gene after substitution are indicated. **d**, The effect of in silico replacement by (CA)_n repeats or random sequences of the same length on the predictions of the CNN model. For each ANG, 50 positions spaced evenly across the 1,000 bp region upstream of the TSS were individually tested for replacement. The distance between adjacent (CA)₈ repeats was 20 bp when multiple (CA)₈ repeats were used. **e**, Analogous

plots showing the effect of the NFE2-MAF-binding motif on the predictions. The NFE2-MAF-binding motif and the BATF3-binding motif belong to the TRE-MARE and CRE-CRE subclass of the bZIP family¹⁰, respectively. **f**, Comparison of the lengths of Z-DNA motifs at the promoters of AIRE-induced genes ($n = 1,747$) versus ANGs ($n = 1,520$). **g, h**, The proportion of AIRE-induced genes among weakly expressed genes (Methods) that have Z-DNA motifs of varying lengths (**g**; the red line) or Z-DNA motifs of varying distances relative to the TSS (**h**; the red line). The dotted grey lines indicate the percentage of AIRE-induced genes ($n = 1,563$) among all of the weakly expressed genes ($n = 4,537$). P values were calculated using two-tailed Wilcoxon rank-sum tests (**f**) and Spearman correlation (**g** and **h**). ANG, AIRE-neutral gene; TPM, transcripts per million.

In silico saturation mutagenesis (ISM) inspects the influence of every nucleotide in an input sequence on a prediction of interest by analysing how single-nucleotide substitutions of it impact the prediction⁶. This approach also identified (CA)_n repeats and the NFE2-MAF-binding motif as features that affect AIRE’s target-gene specificity (Fig. 1b,c and Extended Data Fig. 2b). By contrast, simple motif-enrichment analysis could not identify these two DNA features as being relatively enriched in the extended-promoter sequences of AIRE-induced genes compared with AIRE-neutral genes (Extended Data Fig. 2c). (CA)_n repeats are well known to be Z-DNA-forming sequences¹¹; in general, alternating purine-pyrimidine tracts are sequences with high potential to form Z-DNA¹². We therefore also examined whether the Z-DNA scores computed by an independent Z-DNA prediction model, Z-DNABERT¹³, were sensitive to in silico single-nucleotide mutations in the (CA)_n repeats at promoters of AIRE-induced genes. This indeed proved to be the case (Extended Data Fig. 2d,e).

To further confirm that Z-DNA-forming and NFE2-MAF-binding motifs were predictive of AIRE-induced loci, we randomly selected hundreds of genes originally classified in our model as AIRE neutral and then, for each gene, replaced part of the input sequence at varying positions with a (CA)_n repeat or an NFE2-MAF-binding motif, which would address whether these motifs were sufficient for the input sequence to be reclassified as being AIRE-induced. For (CA)_n repeats, various replacement settings were tested, including single, double or triple (CA)₈ repeats and a single (CA)₁₆ repeat. The longer and more TSS-proximal (CA)_n repeats were more likely to ‘convert’ AIRE-neutral genes into AIRE-induced genes in silico (Fig. 1d). In comparison, replacement with random sequences of the same length did not significantly influence the model’s predictions. Replacements with NFE2-MAF-binding motifs resulted in a somewhat smaller impact

(Fig. 1e), but this effect was still significant in comparison to replacement by a bZIP-family-binding motif not enriched in the strongly positive gradient regions, that is, the BATF3-binding motif.

We next identified all of the Z-DNA motifs at promoters of AIRE-induced and AIRE-neutral genes. The former set had significantly longer Z-DNA motifs compared with the latter (Fig. 1f and Supplementary Table 2). To examine which quantitative features of Z-DNA-forming motifs were most predictive of AIRE-induced genes, we tested how the length and distance from the TSS of Z-DNA-forming motifs were associated with the likelihood of a weakly expressed gene to become AIRE-induced. Specifically, we quantified the percentage of AIRE-induced genes among weakly expressed loci that had Z-DNA motifs of varying lengths and of varying distances from TSSs. There was an increasingly higher percentage of AIRE-induced genes among the entire pool of weakly expressed loci with longer Z-DNA motifs (Fig. 1g). The relative distances of Z-DNA motifs to the TSSs had a negative impact on AIRE’s targeting preferences (Fig. 1h), consistent with results from the in silico sequence-replacement experiments (Fig. 1d).

Leveraging natural genetic variation

As an orthogonal approach to investigating AIRE’s *cis*-regulatory mechanisms, we leveraged natural genetic variation between the B6 and NOD mouse strains to systematically examine the contribution of *cis*-regulation to AIRE-induced gene expression (NOD rather than the more typical CAST/Eij (CAST) comparator was chosen because of its propensity to develop autoimmunity). We generated F1 hybrids by crossing NOD and B6 mice, and performed genome-wide RNA sequencing (RNA-seq) and assay for transposase accessible chromatin with high-throughput sequencing (ATAC-seq) analyses of medullary

thymic epithelial cells (mTECs) from the two parental strains and their offspring (Extended Data Fig. 3a,b and Supplementary Table 3). We then examined the effects of naturally occurring genetic variants, including single-nucleotide polymorphisms (SNPs) and insertions and deletions (indels), on the transcription and chromatin accessibility of AIRE-induced genes. There are approximately 5.1 million SNPs and indels in the NOD versus B6 genomes¹⁴, enabling us to unbiasedly examine, for each TF-binding motif, which sequence variants were associated with allelic imbalances in chromatin accessibility and expression of nearby AIRE-induced genes (Extended Data Fig. 3c). Allelically imbalanced open chromatin regions (OCRs) and gene transcripts were identified using the beta-binomial test. Overall, we identified 3,750 imbalanced OCRs and 1,975 imbalanced gene transcripts (Extended Data Fig. 3d).

There was a substantial positive correlation between the fold changes in chromatin accessibility of the two parental strains and the allelic imbalances in chromatin accessibility of the F1 hybrids (Extended Data Fig. 3e), suggesting that the differential chromatin accessibilities of mTECs from B6 versus NOD mice were primarily *cis*-regulated, as has been reported for other cell types⁵. Moreover, 77% of genes expressed differentially between B6 and NOD mTECs were regulated in *cis* because their expression differences in the two parental strains were recapitulated as allelic imbalances in F1-hybrid mTECs (Extended Data Fig. 3f). Particularly, there was a strong positive correlation between allelic imbalances in chromatin accessibility at OCRs and expression of the nearest AIRE-induced genes (Extended Data Fig. 3g), indicating that *cis*-regulatory variation was a major contributor to the imbalanced expression of AIRE-induced genes in F1-hybrid mTECs.

For each motif in the CIS-BP database, we scanned the two alleles of the imbalanced OCRs for matches, and assigned each OCR to the allele with which it had the stronger motif match. To determine whether motif variants of this particular TF were associated with the generation of imbalanced OCRs, we compared the allelic imbalance in the ATAC-seq signals at the OCRs that have stronger motif matches with the B6 allele with those that have stronger matches with the NOD allele (Extended Data Fig. 3c). This method revealed that genetic variants in binding motifs of the bZIP-family TFs and in (CA)_n-containing motifs were significantly associated with allelic imbalances in transcript expression and chromatin accessibility of AIRE-induced genes (Fig. 2a). Among the bZIP-family TFs, NFE2L2's motif variants had the strongest association with chromatin accessibility, with an average of around 70% of SNP/indel-overlapping ATAC-seq reads mapping to the allele with the stronger match to the NFE2L2-binding motif. Notably, MAFF, a bZIP-family TF that can form a heterodimer with NFE2L2 to regulate target-gene expression¹⁰, was high among those of which the binding motifs were associated with imbalanced expression of AIRE-induced genes. These two observations suggested that an NFE2-MAF heterodimer (for example, NFE2L2-MAFF) might be a positive influencer of AIRE-induced gene expression: the OCR allele with a stronger match to the NFE2-MAF-binding motif was more accessible and the expression of an AIRE-induced gene was biased to the allele with a stronger match to the NFE2-MAF-binding motif (Fig. 2b and Extended Data Fig. 4a,b).

To explore the associations of motifs not included in the CIS-BP database on allelic imbalances, we performed de novo motif analysis to identify sequences that are enriched in the imbalanced OCRs assigned to AIRE-induced genes. Both the NFE2L2-binding motif and (CA)_n repeats were enriched in the imbalanced OCRs of AIRE-induced genes (Fig. 2c). As an example for the Z-DNA motif, the NOD allele of the promoter of the AIRE-induced gene *Marcks1l* had a longer Z-DNA-forming motif, and the expression of *Marcks1l* was also biased to the NOD allele in the F1-hybrid mTECs (Fig. 2d; additional examples are shown in Extended Data Fig. 4c,d). Although there were other DNA motifs of potential interest, the convergence on Z-DNA-forming and NFE2-MAF-binding motifs in the CNN and F1-hybrid data prompted us to focus on these two elements in subsequent experiments.

Z-DNA is associated with AIRE-induced gene expression

Z-DNA is a noncanonical, left-handed, double-helical form of DNA¹¹. There are tens of thousands of Z-DNA motifs in mammalian genomes^{13,15}, enriched at gene promoters. The lengths of Z-DNA-forming motifs are positively correlated with promoter activities and downstream gene expression, and several studies have demonstrated them to have *cis*-regulatory activity^{12,16–20}. Z-DNA motifs are hotspots of genetic variation in human populations, and contain an excess of expression quantitative trait loci^{12,21}.

We first verified *in vivo* Z-DNA formation at gene promoters in the mTECs of mice with wild-type (WT) *Aire* by performing chromatin immunoprecipitation followed by sequencing (ChIP-seq) using the Z22 antibody²², which recognizes both Z-DNA and Z-RNA (the latter of which was removed during the ChIP-seq procedure; quality-control data are shown in Supplementary Table 3). Genes with higher expression levels generally had stronger Z-DNA signals at their promoters (Fig. 3a), consistent with another study that mapped Z-DNA formation genome-wide¹⁹. Notably, for all four gene sets (binned by expression levels), promoters with Z-DNA-forming motifs exhibited stronger Z-DNA signals compared with those without such motifs, suggesting that alternating purine/pyrimidine tracts (Z-DNA-forming motifs) indeed more readily formed Z-DNA *in vivo*. *In vivo* detection of Z-DNA signals at promoter regions was more dependent on Z-DNA-forming motifs for genes with relatively low expression levels, probably due to the limited availability of energy from negative supercoils induced by active transcription. Given that AIRE-induced genes are generally transcribed at low levels in the absence of AIRE, Z-DNA-forming motifs in their promoters could have a strong impact on their expression. There was clear enrichment both of Z-DNA in AIRE peaks and, vice versa, of AIRE in Z-DNA peaks (Fig. 3b), and AIRE-binding levels were positively correlated with Z-DNA signals within Z-DNA peaks (Fig. 3c).

To directly test the hypothesis that Z-DNA influenced AIRE-induced gene transcription, we enhanced Z-DNA formation in mTECs by intraperitoneal injection of spermidine, which is known to stabilize Z-DNA formation *in vitro* or *in vivo*^{20,23,24}. Flow cytometry analyses 7 days after administration of spermidine confirmed that Z-DNA formation was indeed increased (Extended Data Fig. 5a). Importantly, this spermidine-injection protocol did not affect the number or composition of the major thymic stromal cell or thymocyte compartments (Extended Data Fig. 5b–d). RNA-seq analyses showed that injection of spermidine into *Aire*-KO mice partially rescued the loss of AIRE, as indicated by increased expression of a proportion of the previously assigned AIRE-induced genes (termed AIRE-inducible genes in the absence of AIRE) among those with relatively higher mean expression values (Fig. 3d (arrow); mean expression >16). Specifically, 8.5% of these AIRE-inducible genes had fold changes of greater than 2, while 5.0% had fold changes of less than 0.5. By contrast, we did not see such an effect on the activities of expression-matched AIRE-neutral genes (Fig. 3d). These findings raised the possibility that enhanced Z-DNA formation enabled the recruitment of factors that are required for transcriptional induction through some mechanism that bypassed the need for AIRE, thereby allowing induction of some AIRE-inducible genes in mTECs of *Aire*-KO mice.

We also injected spermidine into *Aire*-WT mice. There were 240 more AIRE-induced genes (fold change >2, $P < 0.05$) after spermidine injection than after control injection of phosphate-buffered saline (PBS) (Extended Data Fig. 6a (left)). In this context, most of the spermidine-induced genes were expressed at low levels after PBS treatment (Extended Data Fig. 6a (right)), suggesting that Z-DNA formation enabled AIRE to upregulate the expression of more genes with low basal levels of transcription.

To better understand the effect of spermidine on AIRE-induced gene expression, we performed single-cell RNA-seq (scRNA-seq) analysis of

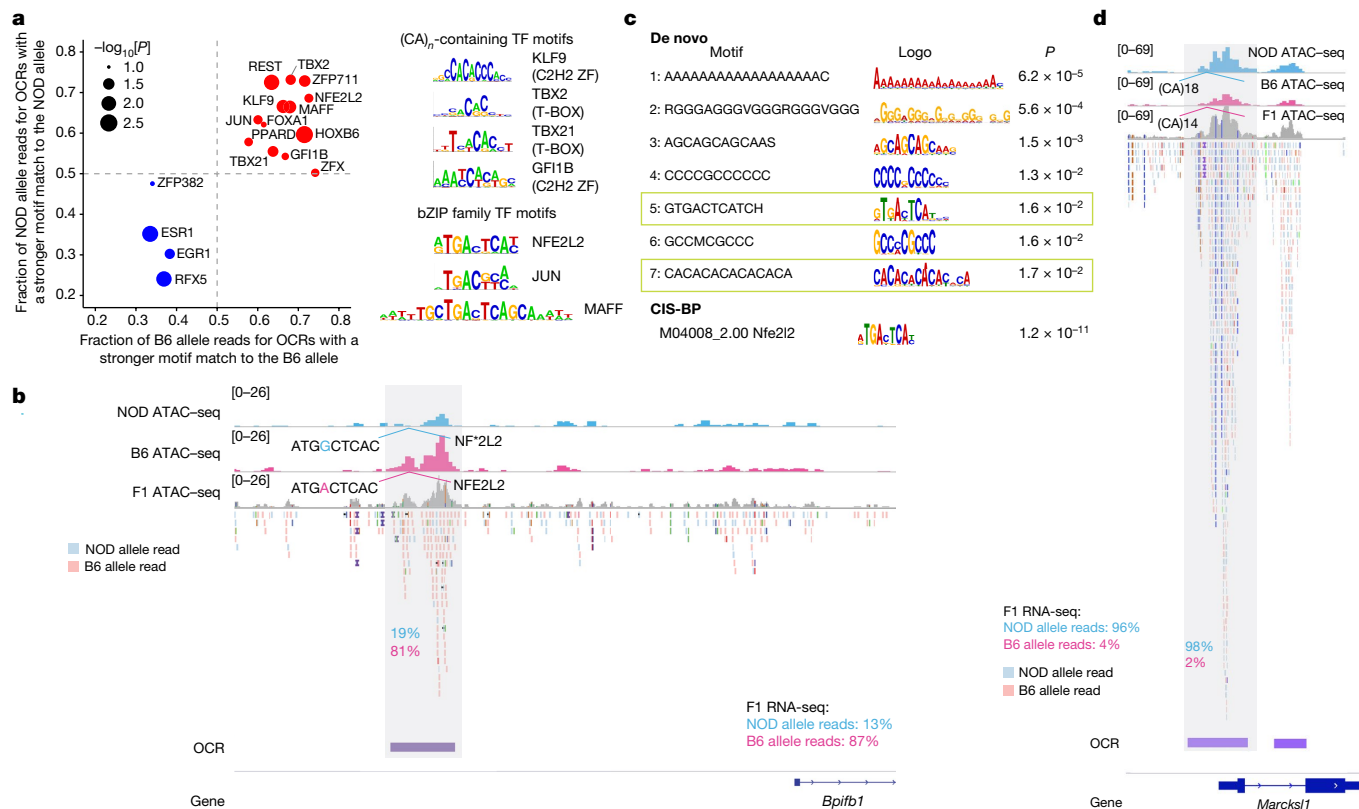


Fig. 2 | Identification of TF-motif variants associated with allelic imbalances in the chromatin accessibility and expression of AIRE-induced genes. **a**, TFs associated with allelic imbalance at the gene transcript level and chromatin accessibility of AIRE-induced genes. The red and blue dots represent potential positive and negative regulators, respectively. TFs with $P < 0.1$ are shown. **b**, An example of a genetic variant of the NFE2L2-binding motif associated with imbalanced OCR accessibility and expression of an AIRE-induced gene. There is an intact NFE2L2-binding motif in the OCR of *Bpifb1* on the B6 allele, which is

disrupted in the NOD allele due to an A to G conversion (marked by the asterisk*). **c**, Motif-enrichment analysis for imbalanced OCRs associated with AIRE-induced genes ($n = 757$). **d**, An example of a genetic variant of a Z-DNA motif associated with allelic imbalance in OCR accessibility and expression of an AIRE-induced gene. At the promoter of *Marcks1*, the NOD allele contained a longer (CA)_n repeat than the B6 allele due to an insertion. P values for TFs in **a** were calculated using two-tailed Wilcoxon rank-sum tests.

the mTEC compartments of PBS- and spermidine-injected *Aire*-WT mice (Extended Data Fig. 6b,c and Supplementary Table 4). We focused on the AIRE-expressing cell clusters that also showed high expression of major histocompatibility complex class II (MHC-II) genes (also known as mTEC^{hi}) (Extended Data Fig. 6d). Spermidine treatment did not substantially influence the transcriptome of AIRE-expressing cells; however, there was a significant upregulation of AIRE-induced, although not AIRE-neutral, genes (Fig. 3e), suggesting a collaboration between AIRE and Z-DNA (in this case, to focus the analysis on AIRE-expressing mTECs, AIRE-induced genes were defined by comparing the transcriptomes of AIRE-GFP⁺ mTECs from *Aire*-WT and *Aire*-KO mice, that is, the same bulk B6 RNA-seq datasets that we used for the F1 analyses).

Z-DNA promotes DSBs at AIRE-induced genes

How Z-DNA enhances transcription is not fully clear. Z-DNA structures are inherently fragile and can promote the generation of double-stranded breaks (DSBs), sometimes spreading over a few hundred base pairs^{25,26}. Although the enzyme responsible for Z-DNA-mediated DSB generation remains unclear, strong candidates include DNA topoisomerases (TOPs)²⁵. TOP-generated DNA breaks are enriched at *cis*-regulatory regions, including promoters, enhancers and chromatin loop anchors²⁷. The TOP-reaction cycle sometimes fails to reseal the DNA breaks, leading to their persistence, the recruitment of proteins involved in the DNA-damage response (DDR) and induction of DNA-repair pathways^{28,29}. DNA breaks and DDR proteins regulate multiple aspects of transcription, including promoting initiation. Both

DSBs and TOPs can facilitate de novo recruitment of transcriptional machineries, including Pol II and general TFs³⁰⁻³². Notably, the proteins involved in DSB generation and the DDR are both physically and functionally associated with AIRE in mTECs^{9,33,34}, prompting the hypothesis that Z-DNA affects AIRE’s target choices by promoting DSB generation at the regulatory sequences of AIRE-induced genes.

We profiled the DSBs from both *Aire*-WT and *Aire*-KO mice genome-wide, using the break labelling in situ and sequencing (BLISS) technique (Supplementary Table 5). In mTECs from *Aire*-WT mice, BLISS signals were enriched at the Z-DNA peaks delineated by CHIP-seq and, vice versa, Z-DNA signals were enriched at DSB hotspots (Fig. 4a); plus, there was a positive correlation between the Z-DNA and DSB signal strengths (Extended Data Fig. 7a). In the absence of AIRE, promoters of AIRE-inducible genes that contained more Z-DNA-forming motifs had significantly stronger BLISS signals compared with those without them (Fig. 4b (left)); by contrast, (GA)_n repeats were not positively associated with BLISS signal intensity at the promoters of AIRE-inducible genes (Fig. 4b (right)). There were stronger BLISS signals at promoters of AIRE-inducible genes than those of expression-matched AIRE-neutral genes in mTECs from *Aire*-KO mice (Extended Data Fig. 7b). Thus, Z-DNA was associated with DSB generation at the promoters of AIRE-inducible genes independently of AIRE.

To directly test Z-DNA’s function in enhancing DSB generation, we performed BLISS analysis of spermidine-treated *Aire*-WT mTECs. The DSB hotspots most upregulated by spermidine (fold change >2, $P < 0.1$) were significantly more enriched with Z-DNA-forming motifs compared with those unaffected by spermidine (Extended Data Fig. 7c).

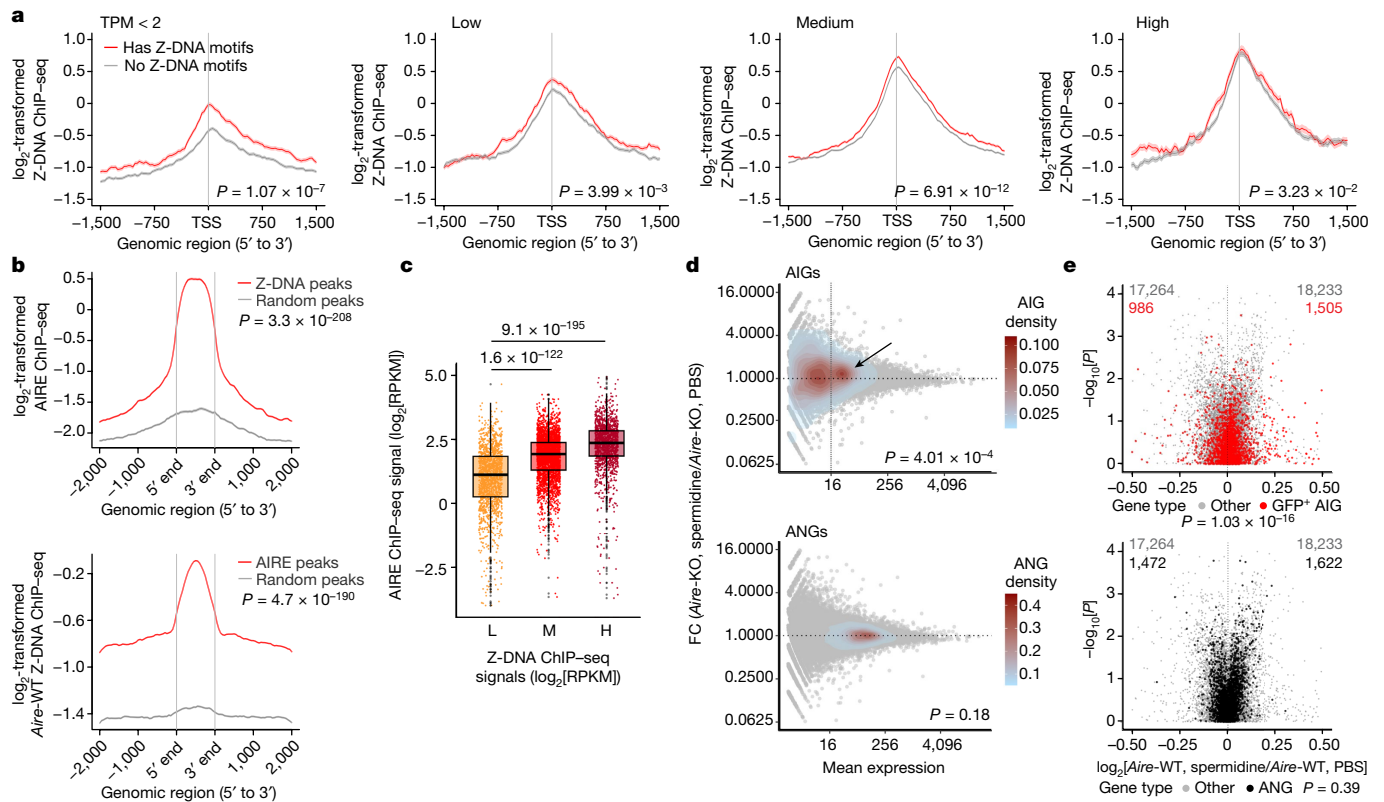


Fig. 3 | Enhancing Z-DNA stability promotes the expression of AIRE-induced genes. **a**, Profiles of Z-DNA ChIP-seq of mTECs from *Aire*-WT mice at promoters of genes with different expression levels. TPM < 2 indicates TPM smaller than 2 in *Aire*-WT mTECs ($n = 5,612$). Low, medium and high represent the bottom 25% ($n = 3,879$), 25–90% ($n = 10,414$) and top 10% ($n = 1,582$) of genes with TPM ≥ 2 . **b**, Profiles of AIRE ChIP-seq at Z-DNA ChIP-seq peaks ($n = 6,022$; top) and vice versa ($n = 37,567$; bottom) versus corresponding random GC-content-matched and size-matched peaks in mTECs from *Aire*-WT mice. Enrichment of ChIP-seq signals in both **a** and **b** were normalized to corresponding IgG controls using the ngs.plot. **c**, Comparison of AIRE ChIP-seq signals at Z-DNA ChIP-seq peaks

that had low, medium or high Z-DNA ChIP-seq signals in mTECs from *Aire*-WT mice. Low, <25th percentile ($n = 1,508$); medium, 25th to 75th percentile ($n = 3,008$); high, >75th percentile ($n = 1,506$). **d**, MA plots of the \log_2 -transformed ratio (M values) versus the \log_2 -transformed average (A values) showing the effect of spermidine treatment on the expression of previously assigned AIRE-induced and AIRE-neutral genes in mTECs from *Aire*-KO mice. **e**, Volcano plots of scRNA-seq for *Aire*-expressing cells from PBS-treated versus spermidine-treated mice. AIRE-induced genes (red; top) and ANGs (dark grey; bottom) are highlighted. P values were calculated using two-tailed Wilcoxon rank-sum tests (**a–c**) and two-tailed Fisher's exact tests (**d** and **e**). FC, fold change; KO, knockout.

By contrast, control CTCF-binding motifs exhibited similar enrichment in upregulated and unaffected DSB hotspots (Extended Data Fig. 7c), again arguing that spermidine treatment could enhance Z-DNA formation, which favoured DSB generation.

In an independent approach to unbiasedly investigate what DNA sequence features influenced DSB generation in mTECs, we performed BLISS analysis of F1-hybrid mTECs generated by crossing CAST and B6 mice. In comparison to the B6 genome, the CAST genome has around 20 million genetic variants¹⁴. We sought to identify TF-binding motifs of which the genetic variants were associated with imbalanced DSB generation on the two alleles of DSB hotspots. CTCF appeared to be a positive regulator of DSB generation as the allele with a stronger match with the CTCF-binding motif had significantly higher DSB signals (Extended Data Fig. 7d). This finding is consistent with studies demonstrating that polymorphisms in CTCF-binding motifs are accompanied by relocation of DSBs at chromatin-loop anchors³⁵, serving to validate our approach. (CA)_n repeats were also positive regulators of DSB generation (Extended Data Fig. 7e). The results from this set of studies prompted us to hypothesize that Z-DNA functions upstream of AIRE to regulate the generation of DSBs at promoters of AIRE-induced genes.

DSBs and promoter poisoning before AIRE action

We profiled chromatin accessibility using ATAC-seq⁹; DNA DSB generation using BLISS; binding of NELF, an indicator of promoter poisoning,

using ChIPmentation; and binding of Ser5-phosphorylated RNA polymerase II (Pol II-pS5), a proxy for Pol II pausing, using cleavage under targets and tagmentation (CUT&Tag) analysis of mTECs from *Aire*-KO versus *Aire*-WT mice. As expected³⁶, promoters of AIRE-inducible genes were poised for expression before AIRE engagement, as indicated by accessible chromatin, NELF binding and Pol II pausing in its absence (Fig. 4c). The decrease in NELF binding in the presence of AIRE was consistent with its ability to release paused Pol II from poised promoters^{36,37}. Promoters of expression-matched AIRE-neutral genes were less accessible and showed less Pol II binding compared with those of AIRE-inducible genes in mTECs from *Aire*-KO mice (Extended Data Fig. 8a). Exemplar profiles are shown for two AIRE-inducible genes and one AIRE-neutral gene that had low basal expression (Extended Data Fig. 8b).

Previous studies have demonstrated the importance of DSBs and TOPs in assisting the disassembly of nucleosomes and assembly of preinitiation complexes at gene promoters^{30–32,38}. In agreement, we observed BLISS signals to be strongly correlated with chromatin accessibility, NELF binding and Pol II binding at AIRE-inducible-gene promoters in mTECs of *Aire*-KO mice (Fig. 4d). High BLISS signals in *Aire*-KO mTECs were also associated with strong recruitment of total Pol II, AIRE and MED1 (a key subunit of the mediator complex required for Pol-II-mediated transcription) in *Aire*-WT mTECs (Extended Data Fig. 8c), and AIRE binding in *Aire*-WT mTECs was positively correlated with Pol II binding at promoters of AIRE-inducible genes in *Aire*-KO mTECs (Fig. 4e). Thus, before the engagement of AIRE, strong DSB

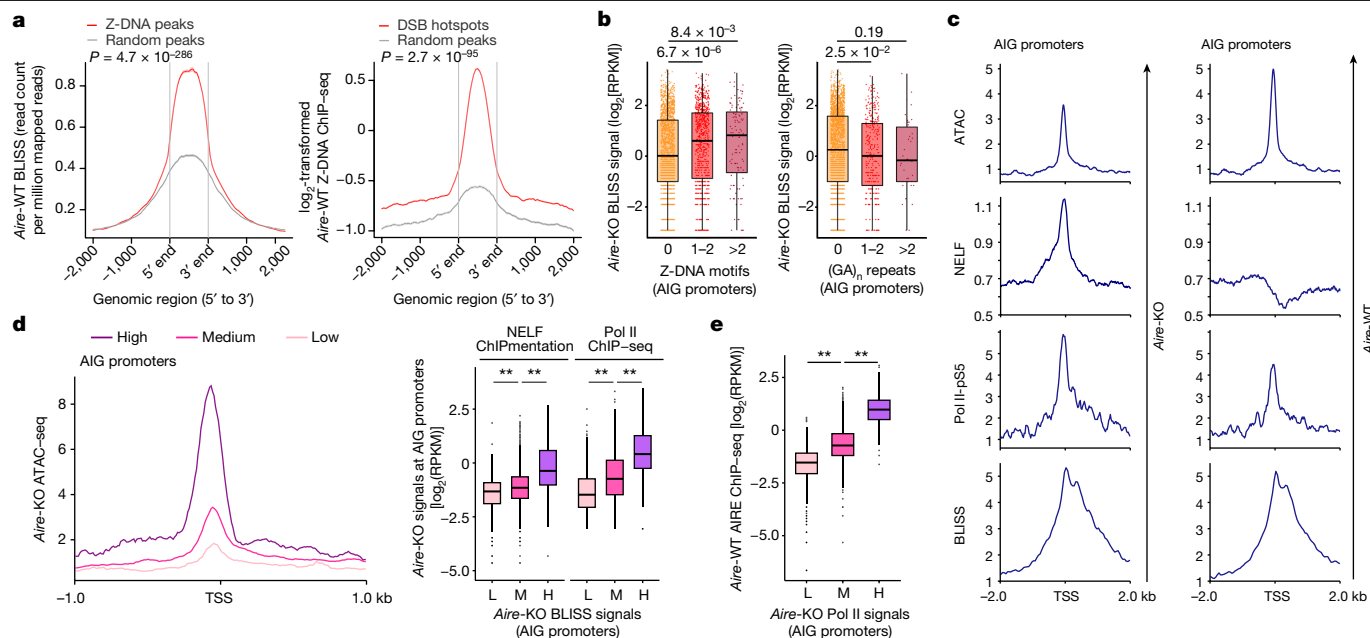


Fig. 4 | Z-DNA motifs are positively associated with the generation of DSBs, the strength of which correlates positively with poisoning of the promoters of AIRE-inducible genes. **a**, Profiles of BLISS at Z-DNA ChIP-seq peaks ($n = 6,022$; left) and vice versa ($n = 21,178$; right) versus corresponding random GC-content-matched and size-matched peaks in mTECs from *Aire*-WT mice. Enrichment of the ChIP-seq signal was normalized to the IgG control. **b**, Comparison of *Aire*-KO BLISS signals between previously assigned AIRE-induced gene promoters with varying numbers of Z-DNA motifs ($n = 2,124, 872$ and 131 for the groups 0, 1–2 and >2 Z-DNA motifs; left) or $(GA)_n$ repeats ($n = 2,719, 367$ and 41 for the groups 0, 1–2 and >2 $(GA)_n$ repeats; right). **c**, Profiles of ATAC-seq, NELF ChIPmentation, Pol II-pS5 CUT&Tag and BLISS

at AIRE-induced gene promoters of mTECs from *Aire*-KO and WT mice. **d**, ATAC-seq, ChIP-seq and ChIPmentation data for sets of AIRE-induced gene promoters that had low (L), medium (M) or high (H) BLISS signals in mTECs from *Aire*-KO mice. **e**, The correlation between Pol II ChIP-seq signals in mTECs from *Aire*-KO mice and AIRE ChIP-seq signals in mTECs from *Aire*-WT mice at AIRE-induced gene promoters. For **d** and **e**, low, <25th percentile; medium, 25th–90th percentile; high, >90th percentile. *P* values were calculated using two-tailed Wilcoxon rank-sum tests (**a**, **b**, **d** and **e**). RPKM, reads per kilobase per million. $n = 747$ (low); $n = 2,130$ (medium); $n = 322$ (high). * $P < 1 \times 10^{-10}$; ** $P < 1 \times 10^{-20}$. Data for WT and *Aire*-KO ATAC-seq, and WT AIRE ChIP-seq are from a previous study⁹.

generation at promoters of AIRE-inducible genes is associated with promoter poisoning and foretells binding of AIRE.

Z-DNA-promoted DSBs enhance promoter poisoning

Topotecan prevents TOP1 from religating the DNA strands that it breaks, thereby enhancing the persistence of DNA breaks³⁹. Topotecan treatment of *Aire*-WT mice significantly increased DSB generation at AIRE-binding sites (Fig. 5a) as well as AIRE binding at promoters of AIRE-induced genes (Fig. 5b). Accordingly, there was a general increase in the expression of AIRE-induced, but not AIRE-neutral, genes after treatment with topotecan (Fig. 5c). More generally, DSB hotspots upregulated by topotecan contained slightly longer Z-DNA-generating motifs compared with those unchanged after topotecan treatment (Fig. 5d).

To further substantiate that Z-DNA regulated promoter poisoning in *cis*, we profiled chromatin accessibility at the promoters of genes subject to AIRE induction in mTECs of *Aire*-KO mice treated with spermidine. Compared with control injection of PBS, administration of spermidine increased the accessibility of such promoters (Fig. 5e).

NFE2L2 affects AIRE-induced gene expression

Both the CNN and F1-hybrid approaches pointed to the NFE2-MAF heterodimer as a second putative regulator of AIRE-induced-gene expression. There are three NFE2-related factors in mice and humans—NFE2L1, NFE2L2 and NFE2L3—all of which are expressed in mTECs. We focused on NFE2L2 because floxed-*Nfe2l2* mice were available and because NFE2L2 is known to induce the expression of some of its target genes by stabilizing nearby Z-DNA formation⁴⁰.

Thus, we examined the correlation between the strength of DSB signals and the presence of NFE2L2-binding motifs at promoters of AIRE-inducible genes in mTECs from *Aire*-KO mice. DSB hotspots containing more NFE2L2-binding motifs had significantly stronger DSB signals compared with those with fewer such motifs; this was not always true of DSB hotspots with CTCF-binding motifs (Extended Data Fig. 9a). Moreover, the DSB hotspots upregulated in mTECs of spermidine-treated *Aire*-WT mice ($FC > 2, P < 0.1$) were more enriched with NFE2L2-binding motifs compared with those unaffected by spermidine (Extended Data Fig. 9b).

Z-DNA-forming motifs and NFE2L2-binding motifs had distinct distribution patterns at DSB hotspots: the former enriched around the centres and the latter concentrated at the boundaries (Extended Data Fig. 9c). This pattern was consistent with previous studies showing that NFE2L2 can stabilize Z-DNA formation nearby, and that the Z-DNA structure propagates into adjacent segments from the central Z-DNA-forming motifs in a cooperative manner^{16–18}. NFE2L2 can stabilize Z-DNA formation by recruiting BRG1¹⁷, a core subunit of the BAF chromatin-remodelling complex. BRG1 stabilizes the energetically unfavourable formation of Z-DNA by using the energy produced by nearby nucleosome ejection^{16,18}. BRG1 was reported to increase the accessibility of *cis*-regulatory elements of AIRE-induced genes, thereby poisoning these loci for expression⁴¹. We reanalysed published ATAC-seq data for mTECs of mice lacking BRG1 (encoded by *Smarca4*) specifically in TECs (and skin) versus WT control mice⁴¹. The OCRs upregulated by BRG1 had longer Z-DNA-forming motifs compared with those unaffected by BRG1 expression (Extended Data Fig. 9d and Supplementary Table 6). Moreover, de novo motif analysis showed that both $(CA)_n$ repeats and NFE2L2-binding motifs were enriched at OCRs

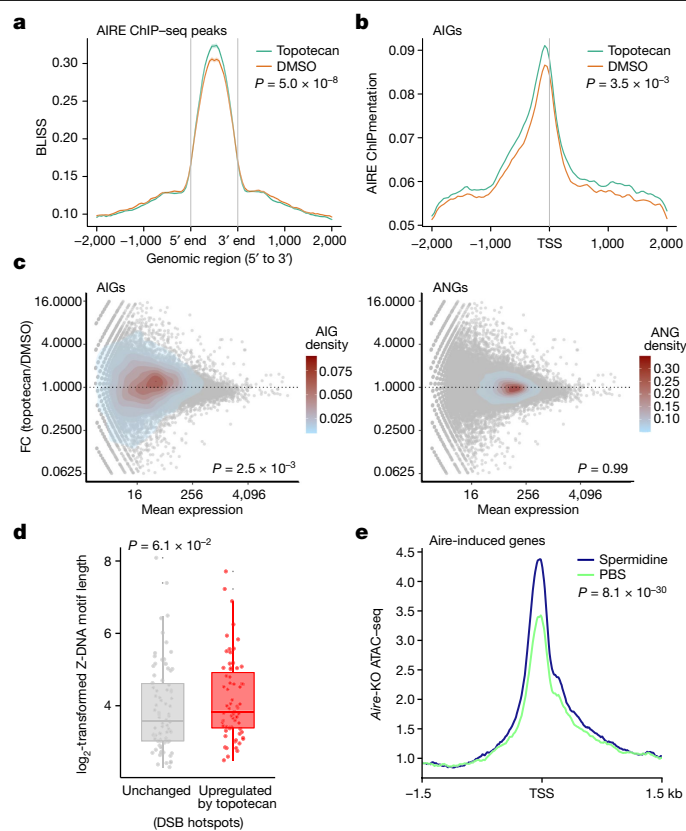


Fig. 5 | DSBs facilitate AIRE-induced gene expression. **a**, BLISS profiles at AIRE ChIP-seq peaks ($n = 37,567$) with or without topotecan treatment. **b**, AIRE ChIPmentation profiles at AIRE-induced gene promoters ($n = 3,231$) with or without topotecan treatment. **c**, MA plots showing the effect of topotecan on AIRE-induced genes and ANG of mTECs from *Aire*-WT mice. **d**, Comparison of the lengths of Z-DNA motifs at DSB hotspots unchanged ($n = 82$) or upregulated (fold change > 2 , $P < 0.1$, $n = 67$) by topotecan in mTECs. **e**, ATAC-seq profiles at promoters of AIRE-induced genes ($n = 3,231$) in mTECs from *Aire*-KO mice treated with spermidine versus PBS. *P* values were calculated using two-tailed Wilcoxon rank-sum tests (**a**, **b**, **d** and **e**) and one-tailed Fisher's exact tests (**c**). DMSO, dimethylsulfoxide.

upregulated by BRG1, while the CTCF-binding motif was increased at OCRs unaffected by BRG1 expression (Extended Data Fig. 9e).

We next compared the transcriptomes of mTECs from *Foxn1^{cre} Nfe2l2^{fllox/fllox}* mice and *Foxn1^{cre} Nfe2l2^{WT/WT}* littermate controls. We first established that the expression of the genes encoding the other two NFE2-related factors was unaffected in these mice (Extended Data Fig. 9f) and that *Nfe2l2*-KO mice had thymic stromal-cell compartments of normal number and composition (Extended Data Fig. 9g). RNA-seq analysis revealed that expression of AIRE-induced genes with NFE2L2-binding motifs at their promoters was slightly more depressed in the absence of *Nfe2l2* compared with the expression of AIRE-neutral genes (Extended Data Fig. 9h). This mild effect may reflect redundancy between NFE2L2 and other family members. More of the differentially expressed loci in *Nfe2l2*-KO mTECs were AIRE induced than AIRE-neutral genes (Extended Data Fig. 9i), suggesting that the lack of NFE2L2 did not generally influence mTEC functions. Notably, the differentially expressed AIRE-induced genes were about half upregulated and half downregulated, indicating that NFE2L2 may not be a general upregulator of AIRE-induced genes, consistent with the limited effect of the NFE2-MAF motif sequence in the *in silico* replacement experiment (Fig. 1e). Together, the two findings suggest that other TFs may cooperate with Z-DNA to regulate AIRE's target specificity.

KEGG pathway analysis of the differentially expressed genes identified a diverse set of mainly downregulated gene modules composed

of AIRE-induced genes (Extended Data Fig. 10a,b). This finding suggested that NFE2L2 might at least partially facilitate AIRE-induced gene expression in a hierarchical manner in which NFE2L2 upregulates the expression of certain TFs that induce the expression of groups of functionally related AIRE-induced genes. It was recently reported that AIRE indirectly induces the expression of groups of functionally related genes encoding peripheral-tissue antigens by promoting the generation of thymic mimetic cells, that is, mTEC subtypes of which the transcriptional programs mimic those of particular peripheral cell types⁴²⁻⁴⁴. The generation of mimetic mTECs depends on the expression of the appropriate lineage-defining TFs, which directly bind to and induce the transcription of sets of peripheral-tissue antigen genes characteristic of their peripheral counterparts⁴². AIRE did upregulate the expression of many lineage-defining TFs in mTECs (Extended Data Fig. 10c). Importantly, NFE2L2 deficiency downregulated the expression of the signature genes of several mimetic mTEC subtypes, including Tuft 1, Tuft 2 and microfold mimetic mTECs (Extended Data Fig. 10d). The downregulated KEGG term 'taste transduction' (Extended Data Fig. 10b) indeed enriches for genes related to Tuft cells. Moreover, spermidine or topotecan injection led to upregulation of the signature genes of several mimetic mTEC subtypes (Extended Data Fig. 10e,f). The overlapping influence on tuft mTEC signature genes between spermidine treatment, topotecan treatment and loss of NFE2L2 suggests that Z-DNA, DSBs and NFE2L2 might cooperate to indirectly regulate the expression of groups of functionally related AIRE-induced genes.

Discussion

The logic of AIRE's target specificity has remained a mystery since its identification as a key regulator of autoimmunity¹. Extended Data Fig. 11 illustrates the Z-DNA-anchored model that we propose, and extensive discussion of the model is provided in Supplementary Discussion. Our findings, coupled with published observations, argue that the strength of AIRE recruitment depends on the abundance of preassembled transcriptional machineries^{3,9,45}. Importantly, AIRE-dependent upregulation of a gene's expression is decoupled from AIRE binding to the gene's promoter—strong AIRE binding does not necessarily lead to AIRE-dependent upregulation. As AIRE cannot perturb the expression of highly transcribed genes that are already robustly induced by TFs, the resulting picture is that AIRE preferentially upregulates the expression of weakly expressed genes, which has often been incorrectly considered to be equal to AIRE preferentially being recruited to weakly expressed or repressed genes. This mindset has greatly impeded identification of the logic underlying AIRE's target specificity.

A growing body of results suggests that Z-DNA, as a form of non-B DNA, is widely involved in transcriptional regulation. Z-DNA-forming motifs are enriched at the promoter regions of a number of genes, influencing their promoter activities and target-gene expression^{12,18-20,40}. It remains to be determined how generally the AIRE-focused mechanism we have identified operates with other genes and in other cell types.

Online content

Any methods, additional references, Nature Portfolio reporting summaries, source data, extended data, supplementary information, acknowledgements, peer review information; details of author contributions and competing interests; and statements of data and code availability are available at <https://doi.org/10.1038/s41586-024-07169-7>.

1. Anderson, M. S. et al. Projection of an immunological self shadow within the thymus by the *aire* protein. *Science* **298**, 1395-1401 (2002).
2. Sansom, S. N. et al. Population and single-cell genomics reveal the *Aire* dependency, relief from Polycarb silencing, and distribution of self-antigen expression in thymic epithelia. *Genome Res.* **24**, 1918-1931 (2014).
3. Meredith, M., Zemmour, D., Mathis, D. & Benoist, C. *Aire* controls gene expression in the thymic epithelium with ordered stochasticity. *Nat. Immunol.* **16**, 942-949 (2015).

4. Brennecke, P. et al. Single-cell transcriptome analysis reveals coordinated ectopic gene-expression patterns in medullary thymic epithelial cells. *Nat. Immunol.* **16**, 933–941 (2015).
5. van der Veecken, J. et al. Natural genetic variation reveals key features of epigenetic and transcriptional memory in virus-specific CD8 T cells. *Immunity*. **50**, 1202–1217 (2019).
6. Novakovsky, G. et al. Obtaining genetics insights from deep learning via explainable artificial intelligence. *Nat. Rev. Genet.* **24**, 125–137 (2023).
7. Kelley, D. R. et al. Sequential regulatory activity prediction across chromosomes with convolutional neural networks. *Genome Res.* **28**, 739–750 (2018).
8. Link, V. M. et al. Analysis of genetically diverse macrophages reveals local and domain-wide mechanisms that control transcription factor binding and function. *Cell* **173**, 1796–1809 (2018).
9. Bansal, K., Yoshida, H., Benoist, C. & Mathis, D. The transcriptional regulator Aire binds to and activates super-enhancers. *Nat. Immunol.* **18**, 263–273 (2017).
10. Rodriguez-Martinez, J. A. et al. Combinatorial bZIP dimers display complex DNA-binding specificity landscapes. *eLife*. **6**, e19272 (2017).
11. Rich, A., Nordheim, A. & Wang, A. H. The chemistry and biology of left-handed Z-DNA. *Annu. Rev. Biochem.* **53**, 791–846 (1984).
12. Georgakopoulos-Soares, I. et al. High-throughput characterization of the role of non-B DNA motifs on promoter function. *Cell Genom.* **2**, 100111 (2022).
13. Umerenkov, D. et al. Z-flipon variants reveal the many roles of Z-DNA and Z-RNA in health and disease. *Life Sci. Alliance* **6**, e202301962 (2023).
14. Keane, T. M. et al. Mouse genomic variation and its effect on phenotypes and gene regulation. *Nature* **477**, 289–294 (2011).
15. Kouzine, F. et al. Permanganate/S1 nuclease footprinting reveals non-B DNA structures with regulatory potential across a mammalian genome. *Cell Syst.* **4**, 344–356 (2017).
16. Liu, R. et al. Regulation of CSF1 promoter by the SWI/SNF-like BAF complex. *Cell* **106**, 309–318 (2001).
17. Zhang, J. et al. BRG1 interacts with Nrf2 to selectively mediate HO-1 induction in response to oxidative stress. *Mol. Cell. Biol.* **26**, 7942–7952 (2006).
18. Liu, H., Mulholland, N., Fu, H. & Zhao, K. Cooperative activity of BRG1 and Z-DNA formation in chromatin remodeling. *Mol. Cell. Biol.* **26**, 2550–2559 (2006).
19. Shin, S. I. et al. Z-DNA-forming sites identified by ChIP-seq are associated with actively transcribed regions in the human genome. *DNA Res.* **23**, 477–486 (2016).
20. Marshall, P. R. et al. Dynamic regulation of Z-DNA in the mouse prefrontal cortex by the RNA-editing enzyme Adar1 is required for fear extinction. *Nat. Neurosci.* **23**, 718–729 (2020).
21. Fotsing, S. F. et al. The impact of short tandem repeat variation on gene expression. *Nat. Genet.* **51**, 1652–1659 (2019).
22. Zhang, T. et al. ADAR1 masks the cancer immunotherapeutic promise of ZBP1-driven necroptosis. *Nature* **606**, 594–602 (2022).
23. Thomas, T. J., Gunnia, U. B. & Thomas, T. Polyamine-induced B-DNA to Z-DNA conformational transition of a plasmid DNA with (dG-dC)_n insert. *J. Biol. Chem.* **266**, 6137–6141 (1991).
24. Brooks, W. H. Increased polyamines alter chromatin and stabilize autoantigens in autoimmune diseases. *Front. Immunol.* **4**, 91 (2013).
25. Wang, G. & Vasquez, K. M. Z-DNA, an active element in the genome. *Front. Biosci.* **12**, 4424–4438 (2007).
26. Meng, Y. et al. Z-DNA is remodelled by ZBTB43 in prospermatogonia to safeguard the germline genome and epigenome. *Nat. Cell Biol.* **24**, 1141–1153 (2022).
27. Pommier, Y., Sun, Y., Huang, S. N. & Nitiss, J. L. Roles of eukaryotic topoisomerases in transcription, replication and genomic stability. *Nat. Rev. Mol. Cell Biol.* **17**, 703–721 (2016).
28. Puc, J. et al. Ligand-dependent enhancer activation regulated by topoisomerase-I activity. *Cell* **160**, 367–380 (2015).
29. Madabhushi, R. et al. Activity-induced DNA breaks govern the expression of neuronal early-response genes. *Cell* **161**, 1592–1605 (2015).
30. Pessina, F. et al. Functional transcription promoters at DNA double-strand breaks mediate RNA-driven phase separation of damage-response factors. *Nat. Cell Biol.* **21**, 1286–1299 (2019).
31. Sperling, A. S., Jeong, K. S., Kitada, T. & Grunstein, M. Topoisomerase II binds nucleosome-free DNA and acts redundantly with topoisomerase I to enhance recruitment of RNA Pol II in budding yeast. *Proc. Natl Acad. Sci. USA* **108**, 12693–12698 (2011).
32. Shykind, B. M. et al. Topoisomerase I enhances TFIID-TFIIA complex assembly during activation of transcription. *Genes Dev.* **11**, 397–407 (1997).
33. Abramson, J., Giraud, M., Benoist, C. & Mathis, D. Aire's partners in the molecular control of immunological tolerance. *Cell* **140**, 123–135 (2010).
34. Guha, M. et al. DNA breaks and chromatin structural changes enhance the transcription of autoimmune regulator target genes. *J. Biol. Chem.* **292**, 6542–6554 (2017).
35. Canela, A. et al. Genome organization drives chromosome fragility. *Cell* **170**, 507–521 (2017).
36. Giraud, M. et al. Aire unleashes stalled RNA polymerase to induce ectopic gene expression in thymic epithelial cells. *Proc. Natl Acad. Sci. USA* **109**, 535–540 (2012).
37. Oven, I. et al. AIRE recruits P-TEFb for transcriptional elongation of target genes in medullary thymic epithelial cells. *Mol. Cell. Biol.* **27**, 8815–8823 (2007).
38. Durand-Dubief, M. et al. Topoisomerase I regulates open chromatin and controls gene expression in vivo. *EMBO J.* **29**, 2126–2134 (2010).
39. Creemers, G. J., Lund, B. & Verweij, J. Topoisomerase I inhibitors: topotecan and irinotecan. *Cancer Treat. Rev.* **20**, 73–96 (1994).
40. Maruyama, A., Mimura, J., Harada, N. & Itoh, K. Nrf2 activation is associated with Z-DNA formation in the human HO-1 promoter. *Nucleic Acids Res.* **41**, 5223–5234 (2013).
41. Koh, A. S. et al. Rapid chromatin repression by Aire provides precise control of immune tolerance. *Nat. Immunol.* **19**, 162–172 (2018).
42. Michelson, D. A. et al. Thymic epithelial cells co-opt lineage-defining transcription factors to eliminate autoreactive T cells. *Cell* **185**, 2542–2558 (2022).
43. Michelson, D. A. & Mathis, D. Thymic mimetic cells: tolerogenic masqueraders. *Trends Immunol.* **43**, 782–791 (2022).
44. Givony, T. et al. Thymic mimetic cells function beyond self-tolerance. *Nature* **622**, 164–172 (2023).
45. Giraud, M. et al. An RNAi screen for Aire cofactors reveals a role for Hnrnp1 in polymerase release and Aire-activated ectopic transcription. *Proc. Natl Acad. Sci. USA* **111**, 1491–1496 (2014).

Publisher's note Springer Nature remains neutral with regard to jurisdictional claims in published maps and institutional affiliations.

Springer Nature or its licensor (e.g. a society or other partner) holds exclusive rights to this article under a publishing agreement with the author(s) or other rightsholder(s); author self-archiving of the accepted manuscript version of this article is solely governed by the terms of such publishing agreement and applicable law.

© The Author(s), under exclusive licence to Springer Nature Limited 2024

Methods

CNN model architecture

Our model was composed of a main body and a task-specific head. The architectures of the main body and pre-train^{46,47} head were similar to those of the model Basenji2^{7,48}, which is one of the state-of-the-art models for learning the *cis*-regulatory lexicon from mammalian genomes. However, our model's main body had a shorter input length and a higher nucleotide resolution. At the pre-training stage, we trained a multitask CNN model on sequences of 2,048 bp length tiled across the mouse genome to predict read-coverage profiles across the 2,048 bp input sequence for 1,643 functional genomic read-outs from the ENCODE⁴⁹ and FANTOM⁵⁰ projects. Thus, by modelling activities of genomic regulatory sequences as a function of the underlying DNA sequences, parameters of the main body were optimized during pre-training to encode *cis*-regulatory DNA-sequence motif information. Details are provided below.

The main body of the model consisted of three parts. The first part used four convolutional blocks to extract relevant DNA sequence motifs. Each convolutional block comprised the following layers: (1) batch normalization; (2) 1D convolution (width 20 in the first block, width 5 in the following blocks); (3) GELU activation⁵¹; and (4) max pool (width 2). The convolutional blocks reduced the dimension from 2,048 bp to 128 so that each position vector encoded sequence information of 16 bp. The number of filters in the convolutional layers increased from an initial 384 to 768 in the last block. The second part had five repeated blocks containing dilated convolutional layers with residual skip connections^{52,53} to spread information and model long-range interactions across the input DNA sequences. The skip connection technique was used to relieve the difficulty in optimization caused by the vanishing gradient problem. Each dilated convolutional block had the following layers: (1) batch normalization; (2) dilated 1D convolution (width 3, filter 768); (3) GELU activation; (4) batch normalization; (5) 1D convolution (width 1, filter 768); (6) GELU activation; (7) dropout (rate 0.3); and (8) skip connection (add with the block input before step 1). The dilation rate was increased by a factor of 2 at each block. The third part of the main body was a 1D convolution (width 1, filter 1,536) with dropout (rate 0.05) to further summarize DNA motif patterns around each 16 bp region. Thus, the output from the main body was the 128 (length) \times 1,536 (filters) representation of 16 bp windows across the 2,048 bp input DNA sequence.

CNN model pre-train

The model was pre-trained on the same sequencing datasets as Basenji2^{7,48} (https://console.cloud.google.com/storage/browser/basenji_barnyard/data/mouse), and used the same Poisson negative log likelihood loss. In brief, the 1,643 mouse genome datasets included 228 DNase-seq or ATAC-seq datasets, 308 TF ChIP-seq datasets, 750 histone modification ChIP-seq datasets and 357 CAGE datasets. We modified the input DNA sequences of Basenji2 by trimming 1/4 length on each side of the original input sequence, dividing the kept sequence into 2,048 bp subsequences and randomly taking five subsequences from the middle half of each sequence. The modified dataset contained 146,475 training, 11,045 validation and 10,085 test sequences for the mm10 mouse genome.

To predict the read coverage profiles for the 1,643 datasets, the pre-train head used a 1D convolution (width 8, stride 8, filter 1,643) followed by a Softplus activation function to generate a positive value for every position in the output 16 \times 1,643 representation of 128 bp windows.

The pre-training model was implemented in TensorFlow (v1.14.0), and was trained on two Tesla V100 GPU cards. We used a batch size of 128, and we stopped training when the validation loss had not improved for 15 epochs and then returned to the model that had achieved the smallest validation loss. We used the Adam optimizer with a learning rate

1×10^{-4} and default values for hyperparameters β_1 (0.9) and β_2 (0.999). We used 5,000 warm-up steps to linearly increase the learning rate from 0 to 1×10^{-4} .

CNN model fine-tune

The fine-tuning dataset consisted of 3,231 extended-promoter sequences from AIRE-induced genes and 3,121 sequences from expression-matched AIRE-neutral genes in the B6 genome. In total, 80% of the dataset was used for training, 15% for validation and 5% for testing. Extended promoters were defined as 1,024 bp upstream of the TSSs to 1,024 bp downstream of the TSSs. All other promoters in the main text were defined as 1,000 bp upstream of the TSSs to 200 bp downstream of the TSSs. We also included two test sets from the NOD genome. One of them had 2,000 sequences that contained SNPs or indels compared with their B6 counterparts. The other had 261 sequences that were not annotated in the B6 genome. Both NOD test sets were balanced with half sequences from AIRE-induced genes and half from AIRE-neutral genes. Each sequence was a DNA stretch $\pm 1,024$ bp around the TSS. To predict whether the input sequence is from an AIRE-induced or AIRE-neutral gene, the fine-tune head implemented the following operations to transform the representation output by the main body to the probability of input sequence being from an AIRE-induced gene: (1) 1D convolution (width 1, filter 10); (2) dropout (rate 0.5); (3) GELU activation; (4) flatten layer; (5) dense layer (unit 3); (6) GELU activation; (7) dense layer (unit 1); and (8) sigmoid activation.

The fine-tuning model was implemented in TensorFlow (v2.3.0) and trained on one Tesla V100 GPU card to minimize the binary cross-entropy loss. In the first stage of fine-tuning, parameters in the main body were frozen when optimizing the parameters in the fine-tune head. We used a batch size of 8 and Adam optimizer with a learning rate 1×10^{-5} and default values for hyperparameters β_1 (0.9) and β_2 (0.999). The optimal batch size, learning rate and dropout rate were tuned by grid search using validation dataset. We stopped the first-stage training when the validation loss had not improved for 20 epochs and then returned to the model that had achieved the smallest validation loss. We then unfroze the parameters in the last 1D convolutional layer of the main body and trained for another 10 epochs using a small learning rate 1×10^{-7} to slightly adjust parameters in the main body.

CNN model interpretation

To identify the DNA sequence motifs that contributed most to the prediction accuracy of the model, for each input sample in the dataset, we computed the absolute value of the gradient of the output prediction with regard to each input nucleotide using backpropagation. For the one-hot encoded dataset, this is equivalent to the gradient \times input score⁵⁴. As each position in the representation output by the main body represented a 16 bp window in the input sequence, we aggregated the gradient \times input profile for every input sequence by taking the average scores for every 16 bp. Thus, we obtained a vector of 128 elements for every input sequence, containing the contribution scores for the 128 16 bp windows. We then determined the genomic loci that had the two largest positive contribution scores for each input sequence and extracted the DNA sequences centred at these two genomic loci containing ten 16 bp windows. To identify DNA motifs enriched in these large-positive-gradient sequences, we used the XSTREME program ($E \leq 0.05$; minimum width, 6; maximum width, 20)⁵⁵ in the MEME suite (v.5.4.1)⁵⁶ to scan these sequences for both de novo motifs and known TF-binding motifs.

Genes originally classified in our model as AIRE-neutral genes ($n = 583$) out of 3,000 randomly selected genes from the genome were used for the ISM experiment. For ISM, computational mutation was performed for every nucleotide in the 2,048 bp input sequence (6,144 substitutions per sequence) to examine how the mutation affected the AIRE-induced gene prediction. The effect of the substitution, which was called the ISM score in Fig. 1, was measured as

Article

$\log_2[P_0/1 - P_0] - \log_2[P_1/1 - P_1]$, where P_0 is the output of the sigmoid function, the prediction probability for the unaltered sequence, and P_1 for the computationally mutated sequence⁵⁷. To identify DNA motifs enriched in the regions (50 bp in length) with the largest ISM scores, we again used the MEME suite⁵⁶.

In the sequence-replacement experiment, the sequences used were: the Z-DNA motifs, (CA)₈ and (CA)₁₆ as well as their reverse complements; a random control sequence of 16 bp (CTACCTAACGCCCTA) and its reverse complement; a random control sequence of 32 bp (TTGGCCGTTAACGTTTGTCTGCCGGATATTCA) and its reverse complement; the NFE2-MAF-binding motif (ATGACTCAGCA) and its reverse complement; the BATF3-binding motif (TGACGTCAC) and its reverse complement. When calculating the percentage of genes classified as AIRE induced after replacement with some sequence, we took the union of genes that were reclassified as AIRE-induced genes by the neural network due to a replacement by some sequence and by its reverse complement.

In silico mutagenesis using Z-DNABERT

Z-DNABERT computes a Z-DNA score (ranging from 0 to 1) for each nucleotide in the input sequence, reflecting how likely that nucleotide is positioned in a stretch of Z-DNA-forming sequence. (CA)_n repeats with high Z-DNA-forming potential (default parameter values: 'model_confidence_threshold' set to 0.5; and the 'minimum_sequence_length' set to 10 bp) were identified for promoters of AIRE-induced genes using Z-DNABERT ($n = 333$). Then, for every nucleotide in every (CA)_n repeat, we performed in silico mutagenesis (ISM) and calculated the ISM score. A positive ISM score indicates that substitution of the original nucleotide leads to a decreased average Z-DNA score across the (CA)_n repeat. The input sequence to Z-DNABERT was still the entire AIRE-induced gene promoter sequence, with only one nucleotide in the (CA)_n repeat mutated to one of the other three nucleotides each time. This procedure ensured that all of the other local genomic information stayed the same when making predictions.

Example ISM score heat maps showed that disruptions of (CA)_n repeats in most cases led to decreased Z-DNA scores, the one exception being CA to CG substitutions. This finding was consistent with the fact that Z-DNABERT gave high scores to (CG)_n repeats. Distributions of ISM scores for nucleotides at various positions near the boundaries of (CA)_n repeats in AIRE-induced gene promoters showed that ISM scores were significantly larger than 0 at all positions examined.

Z-DNA motif identification

Z-DNA motifs were identified as alternating purine-pyrimidine tracts of at least 10 bp. Specifically, G was followed by C or T for at least 10 bp⁵⁸. For the definition of (CA)_n repeats, we used (CA)_n repeats to represent (CA/TG)_n repeats in the main text as (TG)_n on one strand is (CA)_n on the other strand. If (TG)_n repeats occurred in some examples, we also used (CA)_n repeats to describe the result. For example, the (CA)_n repeat at promoter of *Pglyrp4* in Extended Data Fig. 2a was a (TG)_n repeat.

Weakly expressed genes

In the analyses shown in Fig. 1g,h, we focused on weakly expressed genes because both previous^{1,59,60} and the current study found that AIRE upregulates the expression primarily of genes that have low basal expression levels before its action. We defined weakly expressed genes as those with a TPM < 0.35 in mTECs from *Aire*-KO mice ($n = 4,537$). We chose the threshold 0.35 because 50% of AIRE-induced genes have an *Aire*-KO TPM < 0.35 ($n = 1,563$).

Mice

All mice were housed and bred under specific-pathogen-free conditions at the Harvard Medical School Center for Animal Resources and Comparative Medicine (Institutional Animal Care and Use Committee protocol IS00001257).

All experimental mice were 4–6-week-old female mice. The AIRE-deficient mice were described previously¹. Littermates were routinely used for WT and KO comparisons. C57BL/6J (B6) and NOD/ShiLtJ (NOD) mice with *Aire*-driven expression of Igrp-GFP (Adig)⁶¹ were provided by M. Anderson and were appropriately bred to generate *Aire*-GFP⁺*Aire*^{+/+} and *Aire*-GFP⁺*Aire*^{-/-} littermates on the B6, NOD or B6/NOD F1 hybrid backgrounds. CAST/EIJ (CAST) mice were purchased from Jackson Laboratory and bred to B6 mice to generate B6/CAST F1 hybrids. *Foxn1*^{cre} and *Nfe2l2*^{lox/lox} mice were also purchased from Jackson Laboratory and were appropriately bred to generate *Foxn1*^{cre}*Nfe2l2*^{lox/lox} and *Foxn1*^{cre}*Nfe2l2*^{+/+} littermates.

For experiments that used spermidine to enhance Z-DNA formation, 4-week-old B6 *Aire*^{+/+} and *Aire*^{-/-} mice were intraperitoneally injected with 15 mg per kg spermidine (Sigma-Aldrich) in PBS for seven consecutive days. For experiments that used topotecan to stabilize TOP1 binding, 4-week-old B6 *Aire*^{+/+} and *Aire*^{-/-} mice were intraperitoneally injected with 0.5 mg per kg topotecan (Sigma-Aldrich) dissolved in DMSO for three consecutive days. Mice under different intraperitoneal injections were randomly allocated into experimental and control groups.

Isolation, sorting and analysis of thymus cells

Thymus tissues from individual female mice were collected in Dulbecco's modified Eagle medium (DMEM; Gibco) supplemented with 2% fetal bovine serum and 25 mM HEPES (basic medium) and minced with scissors. The fragments were then digested for 20 min with 0.5 mg ml⁻¹ collagenase (Sigma-Aldrich) and 0.2 mg ml⁻¹ DNase (Sigma-Aldrich), then with collagenase/dispase (Roche) and 0.2 mg ml⁻¹ DNase (Sigma-Aldrich) for 15 min. CD45⁺ cells were depleted by magnetic-activated cell sorting (MACS) with CD45 MicroBeads (Miltenyi). For mice on the B6 and B6/CAST background, cells were stained with the following primary antibodies: MHC-II-APC (107614, BioLegend), Ly51-PE (108308, BioLegend); CD45-PE/Cy7 (103114, BioLegend). For mice on the NOD and B6/NOD background, cells were stained with: MHC-II-PE (205308, BioLegend), Ly51-Alexa Fluor 647 (108312, BioLegend); CD45-PE/Cy7 (103114, BioLegend). Cells were stained in the basic medium. 4',6-diamino-2-phenylindole (DAPI) was added before sorting to exclude dead cells. For F1-hybrid sequencing experiments, DAPI⁺CD45⁻Ly51^{low}MHC-II^{high}GFP^{high} mTECs from B6 homozygous, NOD homozygous or B6/NOD F1 mice were sorted on the FACSaria sorter (BD). For all other experiments, DAPI⁺CD45⁻Ly51^{low}MHC-II^{high} mTECs were sorted.

For flow cytometry analysis of thymocytes, the following primary antibodies were used: CD4-Brilliant Violet 605 (100548, BioLegend), CD8a-FITC (100706, BioLegend), CD19-APC (115512, BioLegend). For flow cytometry analysis of Z-DNA formation in mTECs, the anti-Z DNA antibody (ab2079, Abcam) was used.

Mapping of F1 hybrid sequencing reads

We took an unbiased diploid genome alignment strategy to resolve the origin of each read from an F1-hybrid sequencing experiment^{5,62,63}. In brief, we obtained the SNP and indel information for NOD and CAST genome from the Mouse-Genome Project¹⁴, and then modified the B6 genome (mm10) to obtain pseudo-NOD and pseudo-CAST genomes. Sequencing reads were aligned in parallel to both the B6 and the pseudo-NOD or pseudo-CAST genomes. As two alignments for each read were under different coordinate systems, which impeded their direct comparison, we converted the coordinates of alignments in the pseudo-genomes back to the B6 coordinate system. The read was then assigned to the genome where it was uniquely mapped or had a higher mapping score. A read was randomly assigned to the B6 or another genome (NOD or CAST) if it had identical mapping scores for both genomes. The resulting alignment file (BAM) contains genome assignment information for each read, and also has tag indicating how the origin of the read was determined. For genetic-variant-containing reads, they were assigned to a genome in an allele-specific manner. For

reads not covering genetic variants, they were randomly assigned to a genome because of the identical mapping scores.

Statistical testing of allelic imbalance

Only reads overlapping any high-confidence SNP or indel within a gene (RNA-seq), OCR (ATAC-seq) or DSB hotspot (BLISS) were considered when testing for allelic imbalance. We counted the number of variant-overlapping reads from the reference genome (B6), and those from the alternative genome (NOD or CAST), respectively, for every gene, OCR or DSB hotspot using *bcftools*⁶⁴ (v.1.9). Allelically imbalanced regions were identified by modelling allele-specific read-count using the beta-binomial distribution^{62,65}. Specifically, we assumed that the probability of having x_i reads being from the reference or alternative genome for region i followed the beta-binomial distribution $x_i \sim \text{beta-binomial}(n_i, p_i, \theta_i)$ where n_i is the total number of allele-specific reads for region i , p_i indicates the probability of a read being from the reference or alternative genome, and θ_i captures the overdispersion in read count data. For a perfectly balanced region i , $p_i = 0.5$ (null hypothesis). An allelically imbalanced region was identified if p_i was significantly larger or smaller than 0.5. The Benjamini–Hochberg procedure was used to calculate the false-discovery rate.

CIS-BP database

The CIS-BP database⁶⁶ is an online database of TF-binding motifs. It currently hosts data for more than 700 species, over 300 TF families and a total of more than 390,000 TFs. The binding-motif data came from over 70 sources, including Transfac, JASPAR and HOCOMOCO, which are frequently used in TF-binding motif analyses. For *Mus musculus*, the CIS-BP database contains data for 938 TF-binding motifs.

Motif analysis for allelic imbalance

For imbalanced OCRs and DSB hotspots, the alternative-allele (NOD or CAST) sequences were obtained by modifying the corresponding B6-allele sequences using known SNPs and indels¹⁴. We used FIMO⁶⁷ from MEME suite (v.5.4.1) to scan the peak sequences of both the reference and alternative allele for occurrences of TF-binding motifs (match P value $< 1 \times 10^{-4}$) in the CIS-BP database⁶⁶. The coordinates of motifs found in the alternative genome were then converted back to the B6 coordinate system so that the scanning results for two alleles could be merged. We next repeated the following analysis for every TF-binding motif: (1) assign each imbalanced peak to the allele where it had a stronger match as indicated by a smaller FIMO match P value for the particular TF-binding motif; (2) use the nonparametric Wilcoxon rank-sum test to examine whether the allelic ratios of ATAC-seq or BLISS reads from peaks having stronger motif matches on the reference allele were significantly different from those of peaks with stronger motif matches on the alternative allele. De novo motif analysis for imbalanced OCRs was conducted using STREME⁶⁸ ($P < 0.05$; minimum width, 8; maximum width, 20).

RNA-seq library preparation

For each sample, 1,000 cells were sorted directly into the lysis buffer (5 μ l TCL buffer (Qiagen) supplemented with 1% 2-mercaptoethanol (Sigma-Aldrich)). Libraries were constructed according to the Smart-seq2 RNA-seq library preparation protocol, and were then sequenced by the Broad Genomics Platform, according to the standard ImmGen ultra-low-input RNA-seq protocol (<https://www.immgen.org/>).

RNA-seq analysis

For non-F1-hybrid RNA-seq, paired-end RNA-seq reads were aligned to the mm10 genome using STAR⁶⁹. Samples with fewer than 8,000 genes that have more than 10 reads, medium transcript integrity number across all transcripts smaller than 45 or poor intrareplicate correlation were removed from the downstream analyses. Pearson correlations between replicates were calculated using the TPM value

output by Kallisto⁷⁰ (quant, v.0.45.1). MA plots were generated using the \log_2 -transformed fold change and the mean of normalized read counts across all samples for each gene calculated by DESeq2⁷¹ (low expressed genes were removed; v.1.22.2). Differential expression analyses were performed using DESeq2. For F1-hybrid RNA-seq experiments, quality control was performed using Sickle (default settings; v.1.33; <https://github.com/najoshi/sickle>) to remove low-quality reads. Paired-end RNA-seq reads were aligned to the corresponding reference or alternative genome using Tophat2⁷² (v.2.1.1). Only paired-end reads mapped to the single unique genomic location were retained for downstream analysis (SAMtools⁷³; v.1.3.1). Allele-specific read counts were obtained as described above. Gene annotations for the B6 and NOD genome were downloaded from Ensembl release 102 based on the mouse genome assembly GRCm38.

scRNA-seq library preparation

mTEC^{hi} and post-AIRE mTEC^{lo} were sorted from 4–6-week-old female mice based on the gating strategies reported before⁴². Samples were hashed using the TotalSeq-A anti-mouse (anti-CD45/MHC class I) hashtags (BioLegend). Cells were then submitted to the Broad Institute Genomics Platform for encapsulation and library preparation following 10x Genomics protocols.

scRNA-seq analysis

Sequencing reads were demultiplexed, aligned and assigned to cells, and transcript-by-cell matrices were generated using Cell Ranger. CITE-seq-count was used to compute the hash-by-cell matrices. The downstream analyses were largely performed using the Seurat package⁷⁴ (v.4.3.0.1). In brief, hash counts were normalized using the centred log-ratio transformation, and cells were then assigned hash identities by high expression of a single hash. Cells negative for hashtag signals or with multiple hashes were removed. Next, cells with $>10\%$ mitochondrial counts or unique feature counts $> 7,000$ or unique feature count < 200 were removed. Gene expression data were then normalized using the default method LogNormalize. The top 2,000 variable genes were selected using the variance-stabilizing transform (vst) method. After scaling the data, principal component analysis was performed on the top variable genes. The top 50 principal components were retained based on jackstraw and elbow plots for constructing the (shared) nearest-neighbor graph (k.param=20). Cell clustering was first performed using the Louvain algorithm (resolution = 1.55). Then, the top 50 principal components were retained for running the UMAP dimensional reduction. Cell clusters expressing canonical T cell, B cell, myeloid, fibroblast or endothelial markers were removed due to contamination. Cell type annotation was performed on the basis of the expression of marker genes of AIRE-expressing, transit-amplifying, immature and post-AIRE mTECs.

ATAC-seq library preparation

For each ATAC-seq sample, around 15,000 mTECs from 4–6-week-old female mice were sorted into basic medium (described above) for ATAC-seq library preparation, according to the fast-ATAC-seq protocol^{75,76}, which provides high-quality data with low cell input. In brief, cells were centrifuged at 4 °C and washed with 1 ml PBS supplemented with protease inhibitor (Complete EDTA-free protease inhibitor cocktail, Roche). Then, 10 μ l Tn5 transposase mixture was added to resuspend the cell pellet on ice (10 μ l Tn5 transposase mixture: 5 μ l 2 \times Tagment DNA buffer, 0.5 μ l Tagment DNA enzyme from the Nextera DNA Library Preparation Kit (Illumina), 4.4 μ l nuclease-free water, 0.2 mg ml⁻¹ digitonin (G9441, Promega)). Cells were incubated for 30 min at 37 °C with agitation. Transposed DNA fragments were purified using the MinElute Reaction Cleanup Kit (QIAGEN). Two rounds of PCR were performed to generate the library as described in the ImmGen ATAC-seq protocol⁷⁶. After the initial round of PCR with 7 cycles, small DNA fragments were size-selected and purified using the Agencourt

Article

AMPure XP beads (Beckman Coulter) followed by a second round of PCR with 10 cycles. Amplified libraries were purified by AMPure XP beads ($\times 1.8$ vol.) and sequenced on the NextSeq 500 instrument (Illumina) to generate paired-end reads (41 + 40 bp) at the Harvard Medical School Biopolymers Facility.

ATAC-seq analysis

After removing low-quality reads using Sickle and trimming adapter sequences using cutadapt⁷⁷ (v.1.14), we aligned ATAC-seq reads to the corresponding genome (mm10 reference genome, pseudo-NOD genome or pseudo-CAST genome) using bowtie2⁷⁸ (v.2.3.4.3) with the following parameters: `-X 1000 -fr --no-mixed --no-discordant`. Non-uniquely mapped and mitochondrial DNA reads were removed using a combination of SAMtools functions. PCR duplicates were removed using Picard (MarkDuplicates, v.2.8.0; <https://broadinstitute.github.io/picard/>). OCRs for individual samples were identified using MACS2⁷⁹ (callpeak, v.2.1.1.20160309) with the following parameters: `--keep-dup all --nomodel --shift -100 --extsize 200 -p 0.05`. High-confidence, reproducible OCRs among replicates were then identified using the irreproducible discovery rate (IDR) framework⁸⁰ (v.2.0.2) with a global IDR < 0.05. OCRs overlapping ENCODE blacklisted regions were removed from downstream analyses using BEDTools⁸¹ (v.2.27.1). To visualize individual ATAC-seq tracks using the Integrative Genomics Viewer⁸², the alignment file (BAM file) was converted to the read-coverage file (BigWig file) using deepTools⁸³ (bamCoverage, v.3.0.2). ATAC-seq profiles over various genomic regions (for example, TSSs) were generated using the function plotProfile of deepTools or using the ngs.plot⁸⁴ (v.2.47.1). For F1 ATAC-seq, allele-specific read counts for OCRs were obtained as described above.

BLISS library preparation

We followed the suspension-cell BLISS protocol⁸⁵, which is an adaptation of the original BLISS protocol⁸⁶ for non-adherent cells. The entire library preparation process took around 4 days. In brief, on day 1, for each sample, around 100,000 mTECs from 4–6-week-old female mice were sorted into PBS. Cells were fixed in 4% paraformaldehyde (15710, Electron Microscopy Sciences) for 10 min at room temperature on a roller shaker. Formaldehyde was quenched with glycine. Fixed cells were then washed twice using ice-cold PBS. For permeabilization, fixed cells were subjected to two sequential lysis using lysis buffer 1 (10 mM Tris-HCl, 10 mM NaCl, 1 mM EDTA, 0.2% Triton X-100, pH 8) and lysis buffer 2 (10 mM Tris-HCl, 150 mM NaCl, 1 mM EDTA, 0.3% SDS, pH 8). After permeabilization, DSB ends were blunted using the Quick Blunting Kit (E1201L, NEB) for 1 h at room temperature, which was followed by in situ DSB ligation of BLISS adapters using T4 DNA ligase (M0202M, NEB) for around 16 h (overnight) at 16 °C. On day 2, genomic DNAs were reverse cross-linked and extracted using DNA extraction buffer (10 mM Tris-HCl, 100 mM NaCl, 50 mM EDTA, 1% SDS, 1 mg ml⁻¹ proteinase K, pH 8) at 55 °C for around 18 h (overnight) with shaking. On day 3, DNA was purified and then sonicated in 1 \times TE buffer using the Covaris M220 ultrasonicator with the following setting: peak incident power 50, duty factor 10%, cycles per burst 200, time 70 s. After purification using Agencourt AMPure XP beads, DNA was in vitro transcribed using the MEGascript T7 Transcription Kit (AM1333, Thermo Fisher Scientific) at 37 °C for around 14 h (overnight). On day 4, genomic DNA was removed using DNase I (RNase-free) (AM2222, Thermo Fisher Scientific) followed by RNA purification using Agencourt RNAClean XP beads (Beckman Coulter). Libraries were then built through the following steps: Illumina RA3 adapter ligation using T4 RNA ligase 2, truncated KQ (M0373S, NEB) at 25 °C for 2 h; reverse transcription using SuperScript III reverse transcriptase (18080044, Thermo Fisher Scientific) at 50 °C for 1 h; library indexing and amplification using NEBNext High-Fidelity 2 \times PCR Master Mix (M0541S, NEB); DNA purification and size selection (300–800 bp) using Agencourt AMPure XP beads. All primers and adapters were custom synthesized by Integrated DNA Technologies

based on sequences in the TruSeq Small RNA Library Preparation kit (Illumina). BLISS libraries were sequenced on the NextSeq 500 instrument (Illumina) to generate single-end reads (80 bp) at the Harvard Medical School Biopolymers Facility.

BLISS analysis

We used Cutadapt (v.2.5) to scan BLISS reads for matches of the expected 16 bp prefix (8 bp unique molecular identifier (UMI) + 8 bp sample barcode) in the BLISS adapters, allowing a maximum of one mismatch. Only reads containing the 16 bp prefix were retained. Prefixes were then clipped using Cutadapt. Reads were aligned to the corresponding genome (mm10 reference genome or pseudo-CAST genome) using bowtie2 (v.2.3.4.3). Only uniquely mapped reads were retained (SAMtools, v.1.3.1). PCR duplicates that had the same UMIs (allowing for a maximum of two mismatch) were removed using UMI-tools⁸⁷ (dedup, v.1.0.1). DSBs independently generated at the same genomic location in different cells were retained because they had different UMIs. DSB hotspots, defined as peaks identified by HOMER⁸⁸ (findPeaks, v.4.9) with fold enrichment > 1.5 and $P < 1 \times 10^{-5}$, were called for individual samples. DSB hotspots overlapping ENCODE blacklisted regions were removed from downstream analyses using BEDTools (v.2.27.1). DSB hotspots in replicates were merged using BEDOPS⁸⁹ (v.2.4.30) functions and only those occurring in both replicates were retained for further analyses. BLISS profiles over various genomic regions were generated as for ATAC-seq. For B6/CAST F1 BLISS, allele-specific read counts for DSB hotspots were obtained as described above. For differential DSB hotspot analyses, DSB hotspots were called using MACS2⁷⁹ with -p set to 0.1. High-confidence, reproducible peaks among replicates were then identified using the IDR framework⁸⁰ (v.2.0.2) with a global IDR < 0.1. Htseq-count was used to count the number of reads in each DSB hotspot. DESeq2 was then used to perform the differential analyses.

ChIP-seq library preparation

Pol II ChIP-seq libraries were constructed as described previously⁹, and were sequenced on the HiSeq 2500 instrument (Illumina) to generate single-end reads (50 bp). For Z-DNA ChIP-seq, 300,000–500,000 mTECs from 4–6-week-old female mouse were sorted and pooled for each sample. In brief, cells were fixed with 1% formaldehyde (28906, Thermo Fisher Scientific) for 10 min at room temperature with rotation, followed by quenching using 0.125 M glycine for 5 min at room temperature. After washing using ice-cold PBS supplemented with protease inhibitor (Complete EDTA-free protease inhibitor cocktail, Roche), cells were resuspended in lysis buffer (10 mM Tris-HCl pH 8.0, 140 mM NaCl, 1 mM EDTA, 0.1% SDS, 0.1% sodium deoxycholate, 1% Triton X-100) supplemented with protease inhibitor on ice for 10 min. Chromatin was then sonicated on the Covaris M220 ultrasonicator with the following settings: peak incident power 50, duty factor 10%, cycles per burst 200, time 8 min. Lysate was centrifuged for 10 min at 14,000g at 4 °C. An input sample was preserved from the supernatant. The rest of the supernatant was incubated with 2 μ g of anti-Z-DNA/Z-RNA⁹⁰ (Z22) (Ab00783-23.0, Absolute Antibody) or rabbit IgG (2729, Cell Signaling) antibodies precoupled to protein A Dynabeads (Invitrogen) on a rotator overnight at 4 °C. The next day, the beads were washed twice sequentially on a pre-cooled magnet (Invitrogen) using wash buffer 1 (10 mM Tris-HCl pH 8.0, 140 mM NaCl, 1 mM EDTA, 0.1% SDS, 0.1% sodium deoxycholate, 1% Triton X-100), wash buffer 2 (10 mM Tris-HCl pH 8.0, 500 mM NaCl, 1 mM EDTA, 0.1% SDS, 0.1% sodium deoxycholate, 1% Triton X-100), wash buffer 3 (10 mM Tris-HCl pH 8.0, 250 mM LiCl, 1 mM EDTA, 0.5% NP-40, 0.5% sodium deoxycholate) and 1 \times TE. Immunoprecipitated chromatin material on beads was treated with 1 μ g DNase-free RNase (Roche) for 30 min at 37 °C. Beads were then incubated with 50 μ l elution buffer (10 mM Tris-HCl pH 8.0, 300 mM NaCl, 5 mM EDTA, 0.4% SDS) containing 2 μ l proteinase K (NEB) at 55 °C for 1 h and 65 °C overnight to de-cross-link. The next day, DNA was purified using the MinElute Reaction Cleanup Kit (QIAGEN), and

the library was prepared using the NEBNext Ultra II DNA Library Prep Kit for Illumina (NEB) according to the manufacturer's protocol. After purification using AMPure XP beads, the libraries were sequenced on the NextSeq 500 instrument (Illumina) to generate paired-end reads (42 + 42 bp).

ChIPmentation library preparation

For ChIPmentation, each library was constructed using around 50,000 mTECs sorted from a 4–6-week-old female mouse. ChIPmentation libraries were prepared as described previously⁹¹ with some adjustments. In brief, cells were prepared according to the same steps as for ChIP-seq library preparation until the wash step except that (1) the antibodies used were anti-AIRE (14-5934-82, eBioscience) and anti-NELF (ab170104, Abcam); (2) the sonication time was 5 min; and (3) the last wash was performed using 10 mM Tris-HCl pH 8.0 instead of 1× TE. After washing, the beads were then resuspended in 25 µl tagmentation reaction mix with 1 µl Tn5 transposase (Illumina) added, and were incubated at 37 °C for 5 min. After removing the tagmentation reaction mix, the beads were washed twice with wash buffer 1 and once with 1× TE. They were then incubated with 50 µl elution buffer (10 mM Tris-HCl pH 8.0, 300 mM NaCl, 5 mM EDTA, 0.4% SDS) containing 2 µl proteinase K (NEB) at 55 °C for 1 h and 65 °C for 8 h to de-cross-link. DNA was purified using the MinElute Reaction Cleanup Kit (QIAGEN). Libraries were indexed and amplified using the NEBNext High-Fidelity 2× PCR Master Mix (M0541S, NEB) and ATAC-seq primers⁹², followed by purification using AMPure XP beads and sequencing as for ATAC-seq.

ChIPmentation and ChIP-seq analysis

Alignment of ChIPmentation reads was performed as for ATAC-seq reads: trimming low-quality reads, clipping adapters, mapping to the genome, retaining only uniquely mapped reads and removing PCR duplicates (see above). Read-alignment of ChIP-seq datasets was performed as for ATAC-seq except that the adapter-trimming step trimmed different sequences. ChIPmentation and ChIP-seq profiles over various genomic regions were generated also as for ATAC-seq (see above). IgG control for Pol II ChIP-seq of *Aire*-KO mTECs came from a previous study⁹. ChIPmentation and ChIP-seq signals over promoters, defined as -1,000 to 200 bp relative to the TSS, of *Aire*-induced and *Aire*-neutral genes as in Fig. 4d,e and Extended Data Fig. 8c were calculated using the HOMER (v.4.9) script 'annotatePeaks.pl'. Z-DNA ChIP-seq peaks were identified using MACS2⁷⁹ (callpeak, v.2.1.1.20160309) with the following parameters: --keep-dup all -f BAMPE -c ctrl_bam -p 0.1. High-confidence, reproducible peaks among replicates were then identified using the IDR framework⁸⁰ (v.2.0.2) with a global IDR < 0.05. Peaks overlapping ENCODE blacklisted regions were removed from downstream analyses using BEDTools⁸¹ (v.2.27.1).

CUT&Tag library preparation

Libraries were prepared according to a protocol described previously⁹³. In brief, for each sample, 50,000–80,000 mTECs from a female mouse were sorted. After washing in wash buffer 1 (20 mM HEPES pH 7.5, 150 mM NaCl, 0.5 mM spermidine, complete EDTA-free protease inhibitor cocktail), cells were bound to the concanavalin A beads (Bangs Laboratories), followed by incubation with 1:50 primary antibodies (anti-RNA polymerase II phosphorylated at Ser5 (ab5131, Abcam)) in wash buffer 1 supplemented with 0.05% digitonin, 2 mM EDTA and 0.1% BSA at 4 °C overnight. The next day, cells were incubated with 1:100 secondary antibody (guinea pig anti-rabbit IgG, 611-201-122, Rockland) in wash buffer 1 supplemented with 0.05% digitonin at room temperature for 1 h on a rotator. After washing, cells were mixed with 1:200 pA-Tn5 (124601, Addgene; purified in house) in wash buffer 2 (20 mM HEPES pH 7.5, 300 mM NaCl, 0.5 mM spermidine, complete EDTA-free protease inhibitor cocktail) plus 0.01% digitonin at room temperature for 1 h on a rotator. Cells were then washed twice, followed by tagmentation in wash buffer 2 plus 0.01% digitonin and 10 mM MgCl₂ at 37 °C

for 1 h. DNA was solubilized by adding 16.7 mM EDTA, 0.1% SDS and 0.167 mg ml⁻¹ proteinase K to each sample and incubating at 55 °C for 1 h. DNA was phenol-chloroform-extracted and amplified using the NEBNext High-Fidelity 2× PCR Master Mix (M0541S, NEB) and ATAC-seq primers⁹². After purification by AMPure XP beads (×1.3 vol.), the libraries were sequenced as described for ATAC-seq.

CUT&Tag analysis

Quality control, adapter trimming, read alignment and generation of profile plots were performed as described for the ATAC-seq data (see above) except that (1) the bowtie2 parameters used were --local --very-sensitive --no-mixed --no-discordant -X 1000 -fr; and (2) reads were aligned to the *Escherichia coli* genome in parallel to quantify the number of carry-over reads from pA-Tn5.

Z-DNA and NFE2L2-binding motif distribution at DSB hotspots

Z-DNA motifs were identified as alternating purine-pyrimidine tracts of at least 10 bp as described above. NFE2L2-binding motifs in the DSB hotspot were identified using FIMO⁶⁷ from the MEME suite (v.5.4.1). The length of each DSB hotspot was bucketized into 100 position bins. For each position bin of all the DSB hotspots, we counted how many Z-DNA and NFE2L2-binding motifs fell into that bin, and then used the 100 counts to generate the density plots and heat maps as shown in Extended Data Fig. 9c. Curve fitting was performed using polynomial regression.

BRG1 ATAC-seq analysis

GC-content- and quantile-normalized ATAC-seq data for mTEC^{lo} and mTEC^{hi} from *Brg1*-WT and *Brg1*-cKO mice were obtained from the Gene Expression Omnibus (GEO) under accession code GSE102526. OCRs upregulated by BRG1 were defined as (1) mTEC^{hi} *Brg1*-WT ATAC-seq/mTEC^{lo} *Brg1*-WT ATAC-seq > 1.5; and (2) mTEC^{hi} *Brg1*-WT ATAC-seq/mTEC^{hi} *Brg1*-cKO ATAC-seq > 1.5. Unchanged OCRs were defined as (1) mTEC^{hi} *Brg1*-WT ATAC-seq/mTEC^{lo} *Brg1*-WT ATAC-seq > 1.5; and (2) 0.9 < mTEC^{hi} *Brg1*-WT ATAC-seq/mTEC^{hi} *Brg1*-cKO ATAC-seq < 1.1.

KEGG enrichment pathway analysis

The KEGG pathway analysis for differentially expressed genes between mTECs from *Nfe2l2*-KO and control mTECs was performed using the function 'run_KEGG' of the R package clusterProfiler. The cut-off for the enriched pathways was 0.05 for the adjusted *P* value.

Statistical analysis

De novo motif and known TF-motif-enrichment *P* values and *E* values were defined and calculated using the MEME suite, *P* values for bulk RNA-seq differentially expressed genes were calculated in DESeq2 using the Wald test, adjusted *P* values for enriched KEGG pathways were calculated in clusterProfiler using the Benjamini-Hochberg procedure. Box plots show the median (centre line) and the first and third quartiles (box limits), and the upper and lower whiskers of the box plots extended from the hinges to ±1.5 × interquartile range. Other statistical tests were performed using R as specified in the figure legends.

Reporting summary

Further information on research design is available in the Nature Portfolio Reporting Summary linked to this article.

Data availability

All sequencing data reported in this Article have been deposited as a SuperSeries at the GEO under accession code GSE224557. Specifically, the ATAC-seq, BLISS, ChIP-seq, ChIPmentation, CUT&Tag, bulk RNA-seq and scRNA-seq data are available under accession codes GSE224551, GSE224552, GSE224553, GSE224554, GSE224555, GSE224556 and GSE253215, respectively. Public datasets used in this article are as

follows: GSE92594 (ATAC-seq for WT and *Aire*-KO mTECs), GSE92597 (RNA Pol II, AIRE and IgG ChIP-seq for WT mTECs), GSE180937 (MED1 and IgG ChIP-seq for WT mTECs) and GSE102526 (ATAC-seq for mTECs from *Brg1*-WT and *Brg1*-cKO mice). Source data are provided with this paper.

Code availability

Code and scripts used in this study are available at Zenodo (<https://doi.org/10.5281/zenodo.10472904>).

46. Devlin, J., Chang, M.-W., Lee, K. & Toutanova, K. BERT: pre-training of deep bidirectional transformers for language understanding. In *Proc. NAACL-HLT* (eds Burstein, J., Doran, C. & Solorio, T.) 4171–4186 (Association for Computational Linguistics, 2019).
47. Avsec, Z. et al. Effective gene expression prediction from sequence by integrating long-range interactions. *Nat. Methods* **18**, 1196–1203 (2021).
48. Kelley, D. R. Cross-species regulatory sequence activity prediction. *PLoS Comput. Biol.* **16**, e1008050 (2020).
49. Moore, J. E. et al. Expanded encyclopaedias of DNA elements in the human and mouse genomes. *Nature* **583**, 699–710 (2020).
50. Forrest, A. R. et al. A promoter-level mammalian expression atlas. *Nature* **507**, 462–470 (2014).
51. Hendrycks, D. & Gimpel, K. Gaussian error linear units (GELUs). Preprint at arxiv.org/abs/1606.08415 (2020).
52. Jagannathan, K. et al. Predicting splicing from primary sequence with deep learning. *Cell* **176**, 535–548 (2019).
53. He, K., Zhang, X., Ren, S. & Sun, J. Deep residual learning for image recognition. In *Proc. 2016 IEEE Conference on Computer Vision and Pattern Recognition 770–778* (IEEE, Las Vegas, 2016).
54. Simonyan, K., Vedaldi, A. & Zisserman, A. Deep inside convolutional networks: visualising image classification models and saliency maps. Preprint at arxiv.org/abs/1312.6034 (2014).
55. Grant, C. E. & Bailey, T. L. XSTREME: comprehensive motif analysis of biological sequence datasets. Preprint at [bioRxiv https://doi.org/10.1101/2021.09.02.458722](https://doi.org/10.1101/2021.09.02.458722) (2021).
56. Bailey, T. L., Johnson, J., Grant, C. E. & Noble, W. S. The MEME suite. *Nucleic Acids Res.* **43**, W39–W49 (2015).
57. Zhou, J. & Troyanskaya, O. G. Predicting effects of noncoding variants with deep learning-based sequence model. *Nat. Methods* **12**, 931–934 (2015).
58. Cer, R. Z. et al. Non-B DNA v2.0: a database of predicted non-B DNA-forming motifs and its associated tools. *Nucleic Acids Res.* **41**, D94–D100 (2013).
59. Derbinski, J. et al. Promiscuous gene expression patterns in single medullary thymic epithelial cells argue for a stochastic mechanism. *Proc. Natl Acad. Sci. USA* **105**, 657–662 (2008).
60. Peterson, P., Org, T. & Rebane, A. Transcriptional regulation by AIRE: molecular mechanisms of central tolerance. *Nat. Rev. Immunol.* **8**, 948–957 (2008).
61. Gardner, J. M. et al. Deletional tolerance mediated by extrathymic Aire-expressing cells. *Science* **321**, 843–847 (2008).
62. Huang, S. et al. A novel multi-alignment pipeline for high-throughput sequencing data. *Database* **2014**, bau057 (2014).
63. van der Veeken, J. et al. The transcription factor Foxp3 shapes regulatory T cell identity by tuning the activity of trans-acting intermediaries. *Immunity* **53**, 971–984 (2020).
64. Li, H. A statistical framework for SNP calling, mutation discovery, association mapping and population genetical parameter estimation from sequencing data. *Bioinformatics* **27**, 2987–2993 (2011).
65. de Santiago, I. et al. BaalChIP: Bayesian analysis of allele-specific transcription factor binding in cancer genomes. *Genome Biol.* **18**, 39 (2017).
66. Weirauch, M. T. et al. Determination and inference of eukaryotic transcription factor sequence specificity. *Cell* **158**, 1431–1443 (2014).
67. Grant, C. E., Bailey, T. L. & Noble, W. S. FIMO: scanning for occurrences of a given motif. *Bioinformatics* **27**, 1017–1018 (2011).
68. Bailey, T. L. STREME: accurate and versatile sequence motif discovery. *Bioinformatics* **37**, 2834–2840 (2021).
69. Dobin, A. et al. STAR: ultrafast universal RNA-seq aligner. *Bioinformatics* **29**, 15–21 (2013).
70. Bray, N. L., Pimentel, H., Melsted, P. & Pachter, L. Near-optimal probabilistic RNA-seq quantification. *Nat. Biotechnol.* **34**, 525–527 (2016).
71. Love, M. I., Huber, W. & Anders, S. Moderated estimation of fold change and dispersion for RNA-seq data with DESeq2. *Genome Biol.* **15**, 550 (2014).
72. Kim, D. et al. TopHat2: accurate alignment of transcriptomes in the presence of insertions, deletions and gene fusions. *Genome Biol.* **14**, R36 (2013).
73. Li, H. et al. The Sequence Alignment/Map format and SAMtools. *Bioinformatics* **25**, 2078–2079 (2009).
74. Satija, R. et al. Spatial reconstruction of single-cell gene expression data. *Nat. Biotechnol.* **33**, 495–502 (2015).
75. Corces, M. R. et al. Lineage-specific and single-cell chromatin accessibility charts human hematopoiesis and leukemia evolution. *Nat. Genet.* **48**, 1193–1203 (2016).
76. Yoshida, H. et al. The cis-regulatory atlas of the mouse immune system. *Cell* **176**, 897–912 (2019).
77. Martin, M. Cutadapt removes adapter sequences from high-throughput sequencing reads. *EMBnet J.* <https://doi.org/10.14806/ej.17.1.200> (2015).
78. Langmead, B. & Salzberg, S. L. Fast gapped-read alignment with Bowtie 2. *Nat. Methods* **9**, 357–359 (2012).
79. Zhang, Y. et al. Model-based analysis of ChIP-Seq (MACS). *Genome Biol.* **9**, R137 (2008).
80. Qunhua, L., James, B. B., Haiyan, H. & Peter, J. B. Measuring reproducibility of high-throughput experiments. *Ann. Appl. Stat.* **5**, 1752–1779 (2011).
81. Quinlan, A. R. & Hall, I. M. BEDTools: a flexible suite of utilities for comparing genomic features. *Bioinformatics* **26**, 841–842 (2010).
82. Robinson, J. T. et al. Integrative genomics viewer. *Nat. Biotechnol.* **29**, 24–26 (2011).
83. Ramirez, F. et al. deepTools: a flexible platform for exploring deep-sequencing data. *Nucleic Acids Res.* **42**, W187–W191 (2014).
84. Shen, L., Shao, N., Liu, X. & Nestler, E. ngs.plot: quick mining and visualization of next-generation sequencing data by integrating genomic databases. *BMC Genom.* **15**, 284 (2014).
85. Gothe, H. J. et al. Spatial chromosome folding and active transcription drive DNA fragility and formation of oncogenic MLL translocations. *Mol. Cell* **75**, 267–283 (2019).
86. Yan, W. X. et al. BLISS is a versatile and quantitative method for genome-wide profiling of DNA double-strand breaks. *Nat. Commun.* **8**, 15058 (2017).
87. Smith, T., Heger, A. & Sudbery, I. UMI-tools: modeling sequencing errors in Unique Molecular Identifiers to improve quantification accuracy. *Genome Res.* **27**, 491–499 (2017).
88. Heinz, S. et al. Simple combinations of lineage-determining transcription factors prime cis-regulatory elements required for macrophage and B cell identities. *Mol. Cell* **38**, 576–589 (2010).
89. Neph, S. et al. BEDOPS: high-performance genomic feature operations. *Bioinformatics* **28**, 1919–1920 (2012).
90. Möller, A. et al. Monoclonal antibodies recognize different parts of Z-DNA. *J. Biol. Chem.* **257**, 12081–12085 (1982).
91. Schmid, C., Rendeiro, A. F., Sheffield, N. C. & Bock, C. ChIPmentation: fast, robust, low-input ChIP-seq for histones and transcription factors. *Nat. Methods* **12**, 963–965 (2015).
92. Buenostro, J. D. et al. Single-cell chromatin accessibility reveals principles of regulatory variation. *Nature* **523**, 486–490 (2015).
93. Kaya-Okur, H. S. et al. CUT&Tag for efficient epigenomic profiling of small samples and single cells. *Nat. Commun.* **10**, 1930 (2019).
94. Bansal, K. et al. Aire regulates chromatin looping by evicting CTCF from domain boundaries and favoring accumulation of cohesin on superenhancers. *Proc. Natl Acad. Sci. USA* **118**, e2110991118 (2021).

Acknowledgements We thank A. Baysov, J. Lee, I. Magill and the members of the Broad Genomics Platform for RNA-seq and scRNA-seq; the staff at the HMS Biopolymers Facility for all other sequencing; the members of the HMS Immunology Flow Core; L. Du and the staff at the HMS Transgenic Mouse Core; K. Hattori and A. Ortiz-Lopez for experimental assistance; L. Yang and B. Vijaykumar for computational help; C. Laplace for graphics; K. Chowdhary and D. Michelson for discussions; M. Anderson for providing the NOD mice with *Aire*-driven expression of IGRP-GFP; and A. Herbert for drawing our attention to the Z22 monoclonal antibody. This work was supported by NIH grant R01AI088204 (to D.M.). Y.F. is in part supported by the Harvard Molecules, Cells and Organisms Training Program. K.B. is supported by the Department of Biotechnology/Wellcome Trust India Alliance Intermediate Fellowship (IA/1/19/1/504276).

Author contributions Y.F. and D.M. conceived the study. Y.F. designed and performed all experiments except for the Pol II ChIP-seq. Y.F. performed all data analysis with supervision from D.M., C.B. and S.M. K.B. performed the Pol II ChIP-seq of mTECs from *Aire*-KO mice. Y.F. and D.M. wrote the manuscript, which was edited by all of the authors.

Competing interests The authors declare no competing interests.

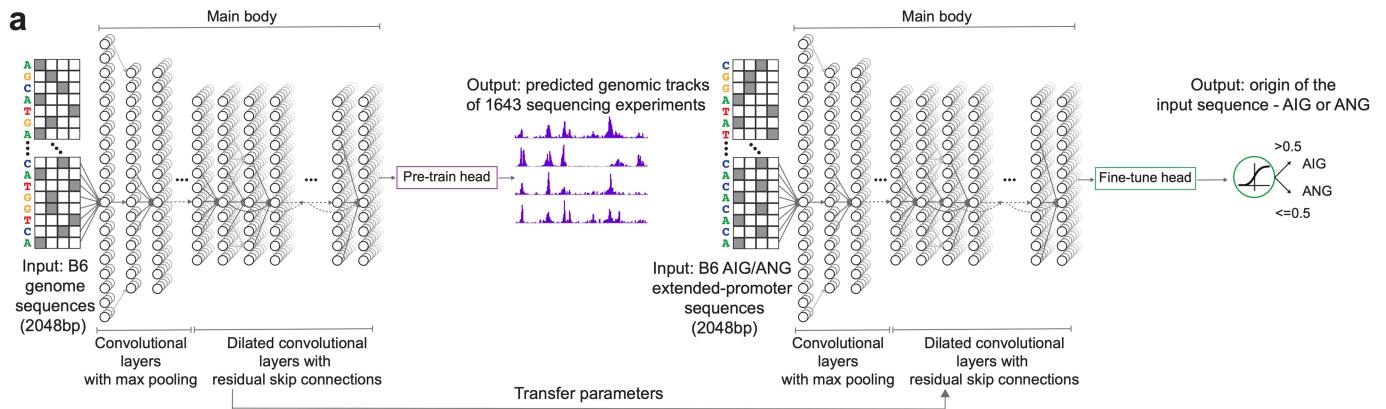
Additional information

Supplementary information The online version contains supplementary material available at <https://doi.org/10.1038/s41586-024-07169-7>.

Correspondence and requests for materials should be addressed to Diane Mathis.

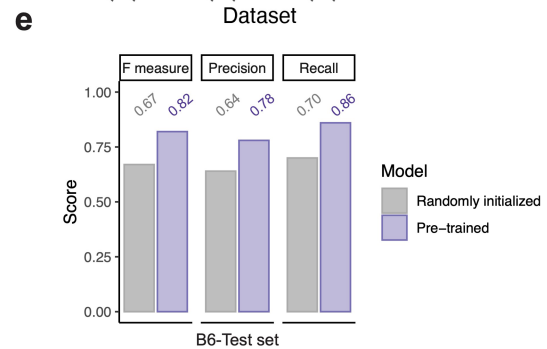
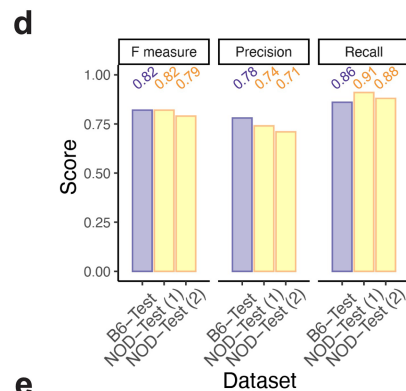
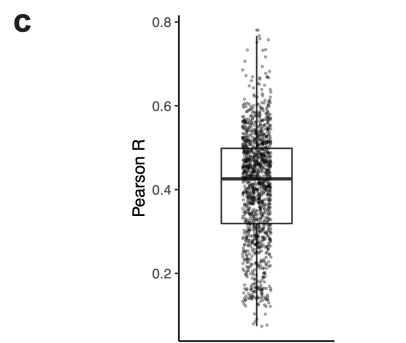
Peer review information *Nature* thanks Alan Herbert and the other, anonymous, reviewer(s) for their contribution to the peer review of this work.

Reprints and permissions information is available at <http://www.nature.com/reprints>.

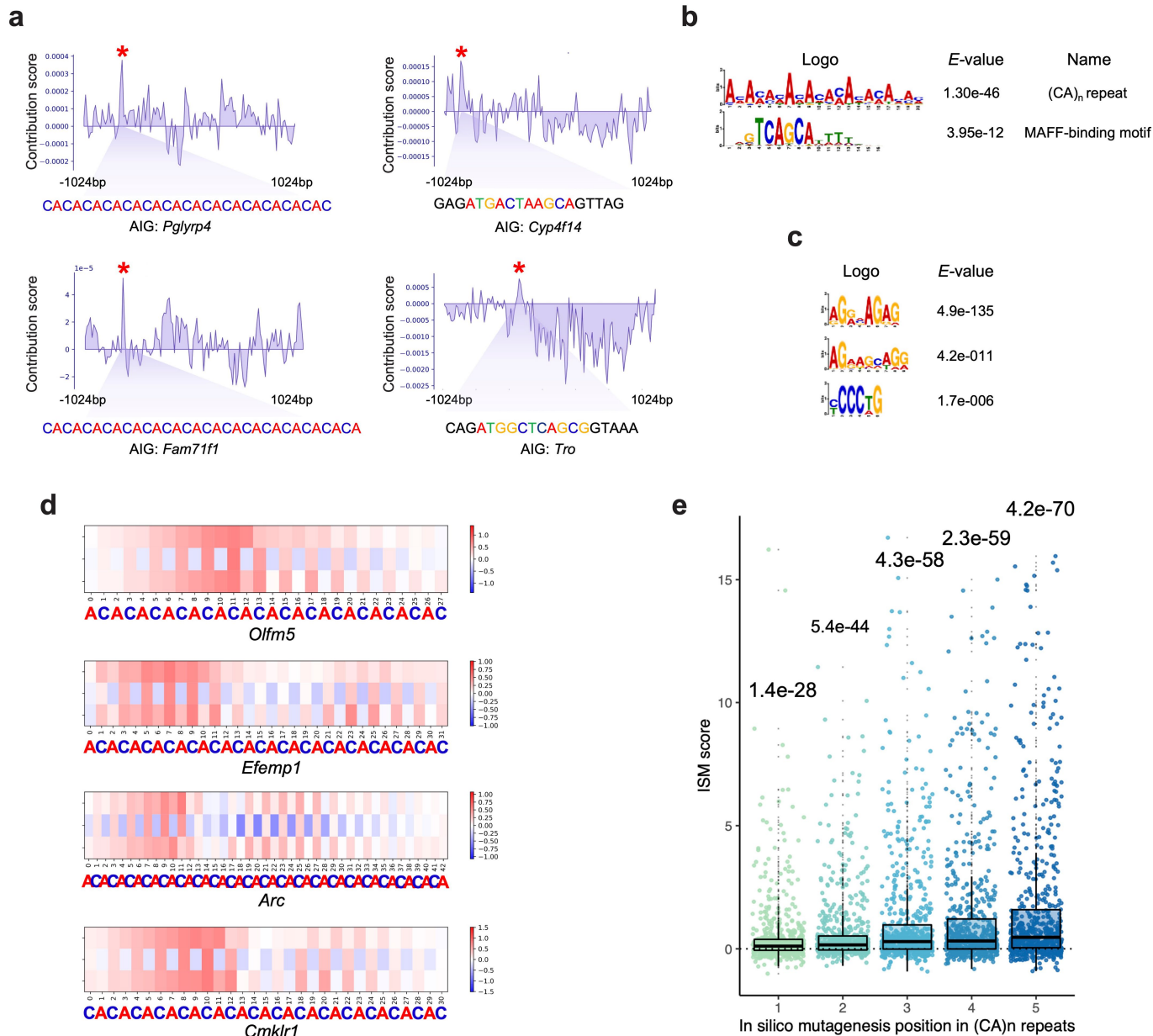


Extended Data Fig.1 | Performance of the pre-trained CNN model.

a, Schematics of the CNN model for pre-training and fine-tuning. The first section of the main body is comprised of convolutional layers to extract relevant DNA sequence motifs. The following section has repeated blocks containing dilated convolutional layers with residual skip connections, to spread information and model long-range interactions in the input DNA sequences. AIRE-induced and expression-matched AIRE-neutral gene lists have been described^{3,9}. Briefly, AIRE-induced genes were defined as $Aire^{+/+}/Aire^{-/-} > 2$ and AIRE-neutral genes were $Aire^{+/+}/Aire^{-/-} > 0.9$ and < 1.1 , based on bulk RNA-seq data from ref. 3. **b**, Exemplar true versus predicted profiles over a randomly selected sequence from the test set. Profiles for 15 sequencing datasets are

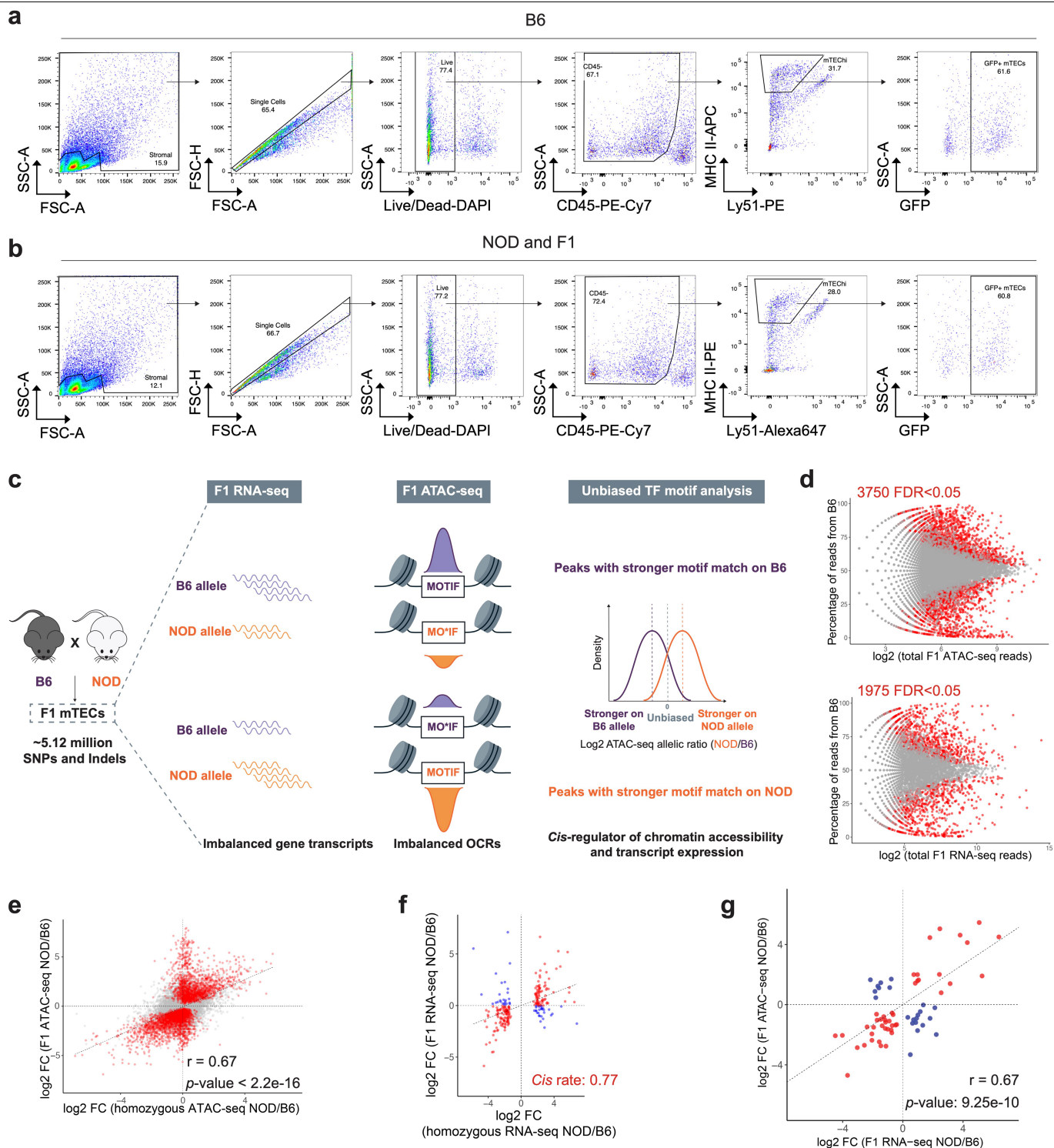


shown. **c**, Boxplot showing the Pearson correlations between the predicted and true sequencing profiles of test set sequences for the sequencing datasets used for the pre-training, including DNase-seq, ATAC-seq and ChIP-seq. **d**, Model evaluation on four datasets: a test set and validation set from the B6 genome, and two test sets from the NOD genome: (1) containing SNPs/Indels compared with counterparts in the B6 genome, and (2) derived from NOD-specific genes (in order to prevent data leakage during prediction). **e**, Bar plot comparing the performances of randomly initialized model and pre-trained model on the test set from the B6 genome. SNPs: single-nucleotide polymorphisms; Indels: insertions and deletions; AIG, AIRE-induced gene; ANG: AIRE-neutral gene.



Extended Data Fig. 2 | Additional analysis using the fine-tuned CNN model and Z-DNABERT, related to Fig. 1. **a**, Contribution score profiles for AIRE-induced genes whose largest-positive-gradient regions contained $(CA)_n$ repeats (left) or NFE2-MAF-binding motifs (right). **b**, Motifs enriched in the regions (50 bp in length) with the largest ISM scores. **c**, Motifs that are relatively more enriched in extended-promoter sequences of AIRE-induced genes than AIRE-neutral genes (E -value < 0.05). The MEME suite was used to identify the enriched motifs for panel **b** and **c**. **d**, Example ISM score heatmaps for $(CA)_n$ repeats in AIRE-induced gene promoters. Each of the three rows shows results

for one possible substitution in the order of A \rightarrow C \rightarrow G \rightarrow T from top to bottom. Red (positive ISM score) indicates that substitution of the original nucleotide leads to a decreased average Z-DNA score across the stretch of the $(CA)_n$ repeat; Blue (negative ISM score) indicates the other way. **e**, Boxplot showing the distribution of ISM scores at various positions near the boundaries of $(CA)_n$ repeats in AIRE-induced gene promoters. For example, position 2 indicates the second nucleotides from both ends of a $(CA)_n$ repeat. p -values for panel **e** were calculated using the one-sample Wilcoxon Signed Rank Test (one-tailed). AIRG, AIRE-induced gene.



Extended Data Fig. 3 | Strain-specific gene expression in mTECs was predominantly driven by *cis*-regulation. a, b, Cytofluorometric gating scheme for isolation of mTECs from B6 (a), NOD and F1 (b) mice. **c**, Rationale of the F1-hybrid analysis. **d**, Allelically imbalanced gene transcripts and OCRs in B6×NOD F1-hybrid mTECs. Red dots depict significantly imbalanced events with a false discovery rate (FDR) < 0.05. **e**, Correlation between the fold-changes in accessibility for mTEC OCRs in B6 versus NOD mice (x axis) and fold-changes in accessibility for OCRs (n = 23256) on the B6 versus NOD allele in mTECs of F1 hybrids (y axis). Red dots depict significantly imbalanced OCRs (n = 3750). **f**, Correlation between the fold-changes in transcript levels for mTECs from B6

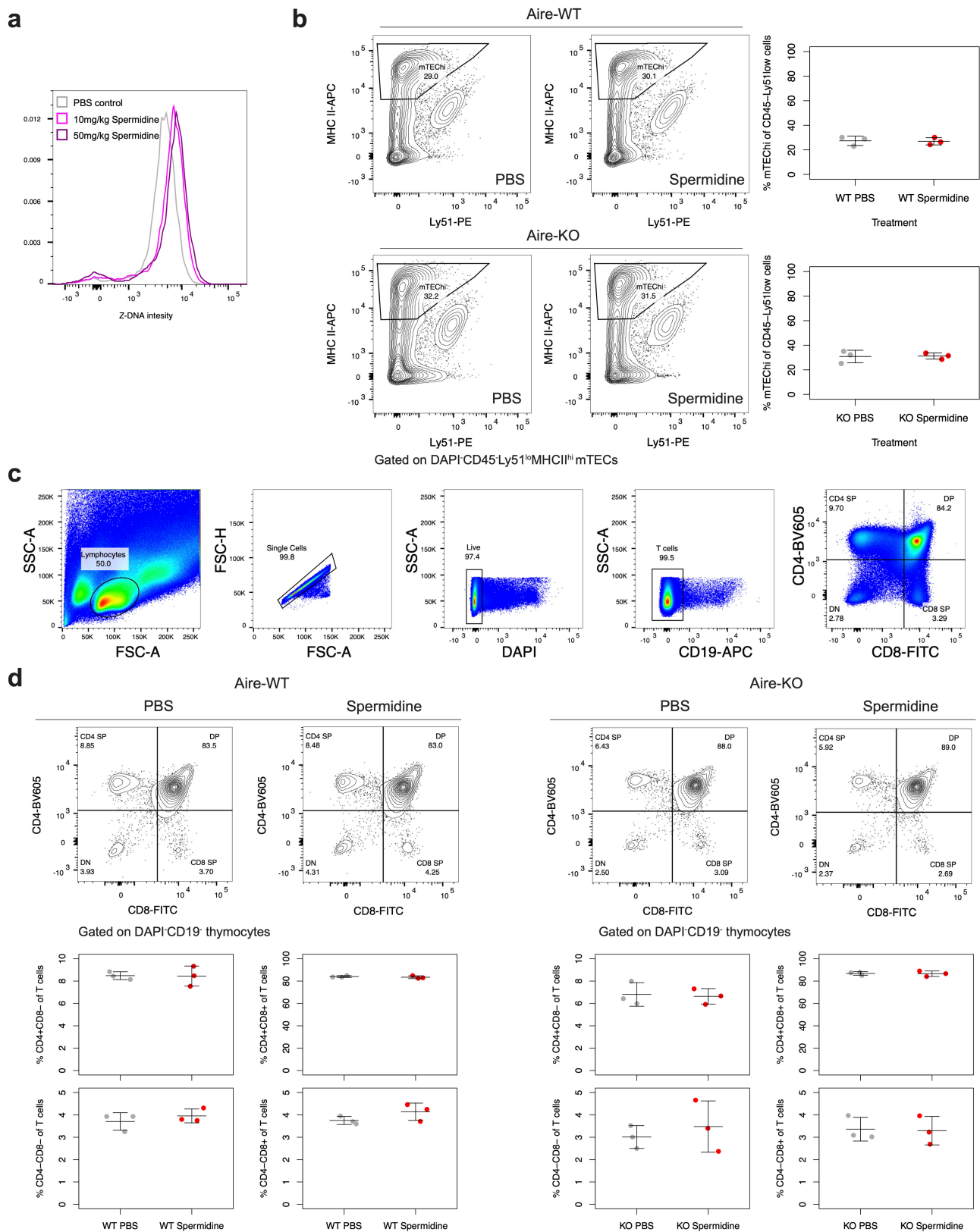
versus NOD mTECs (x axis) and transcript fold-changes for the B6 versus NOD allele in mTECs of F1 hybrids (y axis). Only genes significantly differentially expressed in B6 and NOD mTECs are shown (adjusted *p*-value < 0.05, n = 248). **g**, Correlation between allelic biases in the expression of the nearest AIRE-induced gene (x axis) and in the accessibility of the nearest AIRE-induced gene (y axis). The imbalanced OCR was assigned to an imbalanced AIRE-induced gene (n = 248) if 1) the OCR was located within 50,000 bp of the gene's TSS and 2) the AIRE-induced gene was the OCR's nearest gene. There were 156 imbalanced OCRs assigned to imbalanced AIGs. *p*-values according to panels **e** and **g** were from Spearman's correlation. FC: fold-change. OCR: open chromatin region; TF: transcription factor.

Article



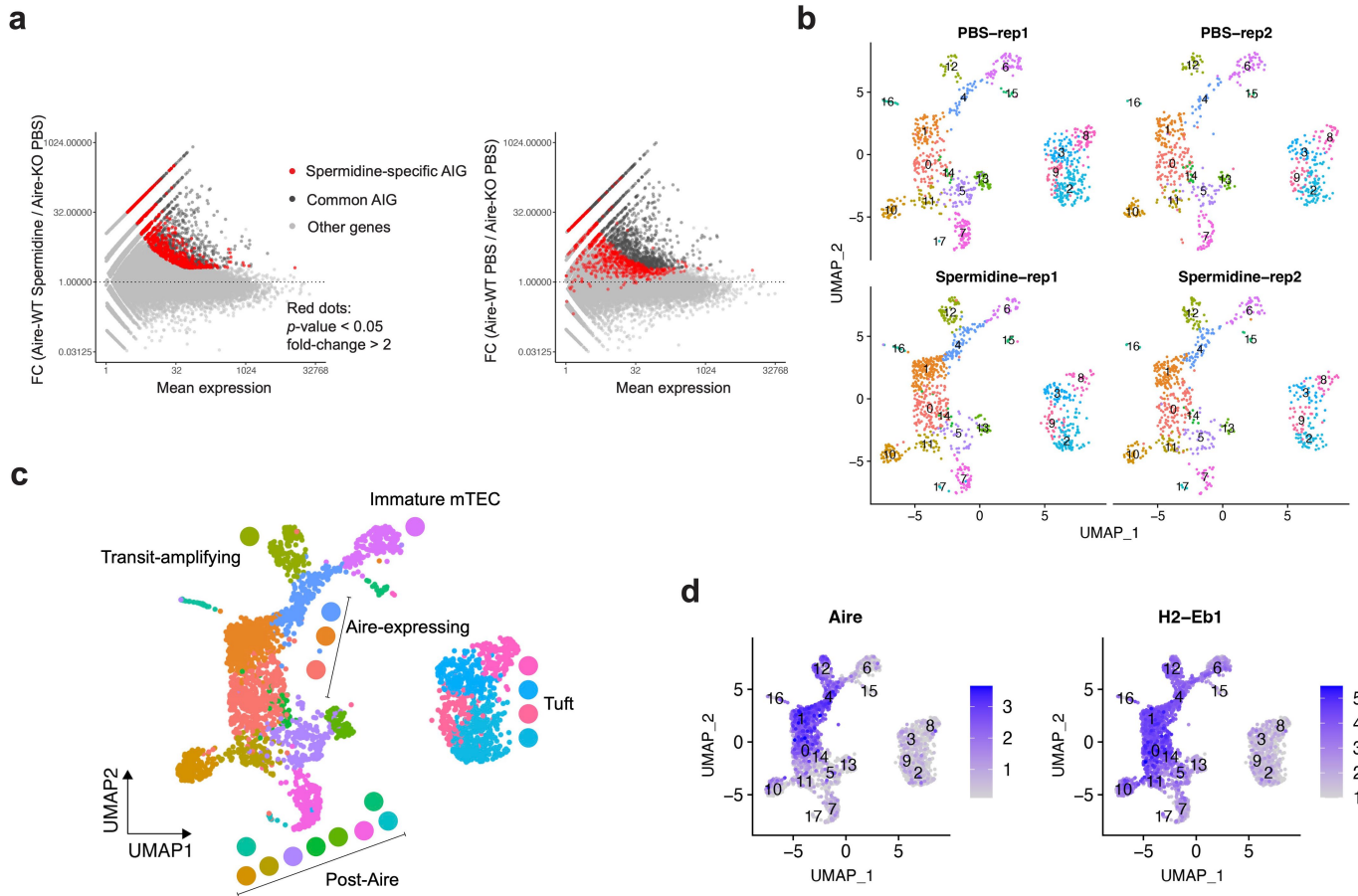
Extended Data Fig. 4 | Exemplar genetic variants associated with allelic imbalances in chromatin accessibility and gene expression. a,b, Examples of genetic variants of NFE2L2-binding motifs associated with imbalanced

expression of AIRE-induced genes. **c,d,** Examples of genetic variants of Z-DNA motifs associated with allelic imbalances in the expression of an AIRE-induced gene. OCR: open chromatin region; WT: wild-type; *Aire*-KO: *Aire* knockout.



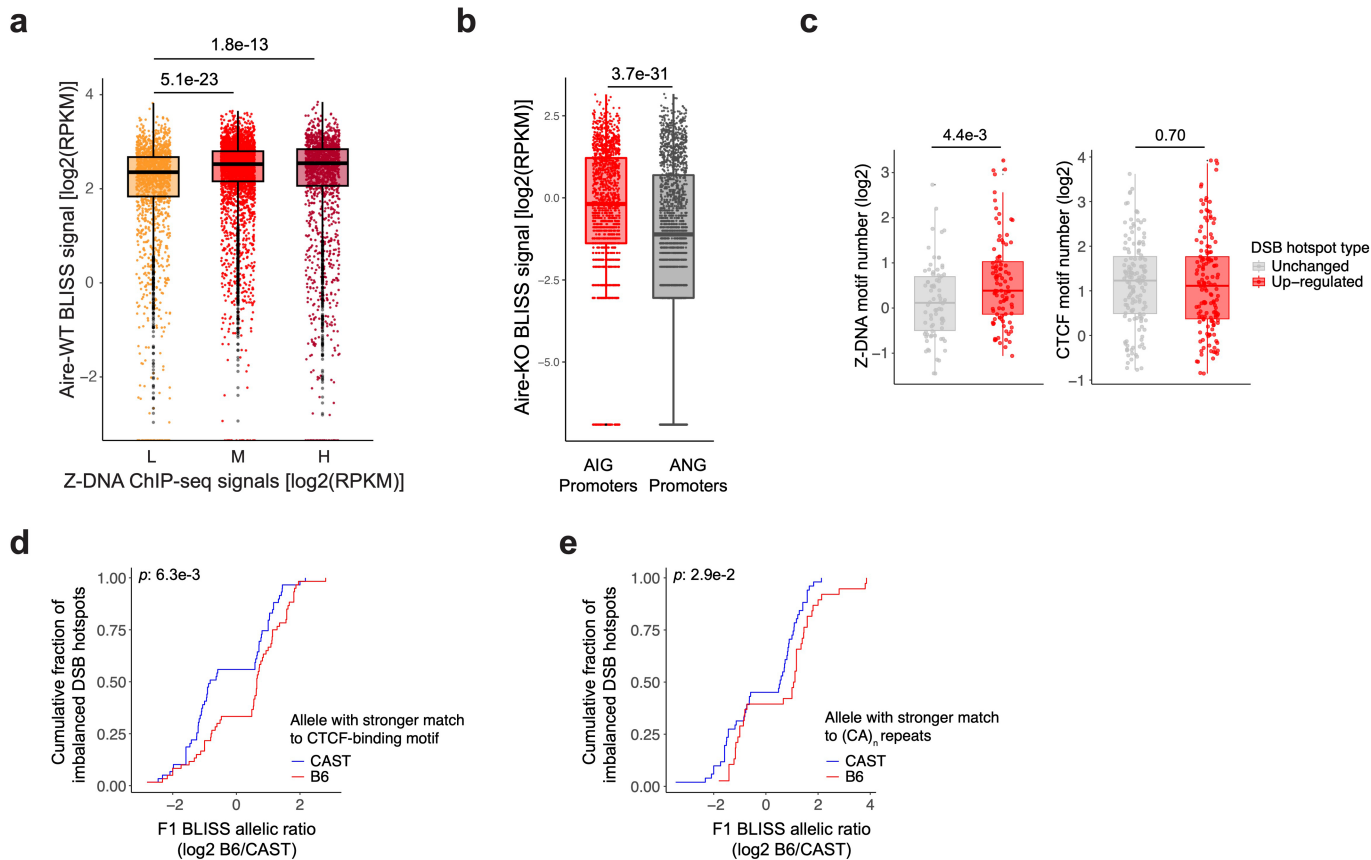
Extended Data Fig. 5 | Effect of spermidine on Z-DNA formation and thymic cell populations. **a**, Density plot showing the effect of spermidine vs control PBS injection on Z-DNA intensity in mTECs measured by flow cytometry using an anti-Z-DNA antibody. **b**, Representative cytofluorimetric plots and quantitative

summary for mTECs of WT and *Aire*-KO mice treated with spermidine or control PBS. **c**, Cytofluorometric gating scheme for analyses of thymocyte compartments. **d**, Analogous plots to panel **b** for thymocyte compartments. Error bars, mean \pm s.e.m. from $n = 3$ biological replicates. KO: *Aire*-KO.



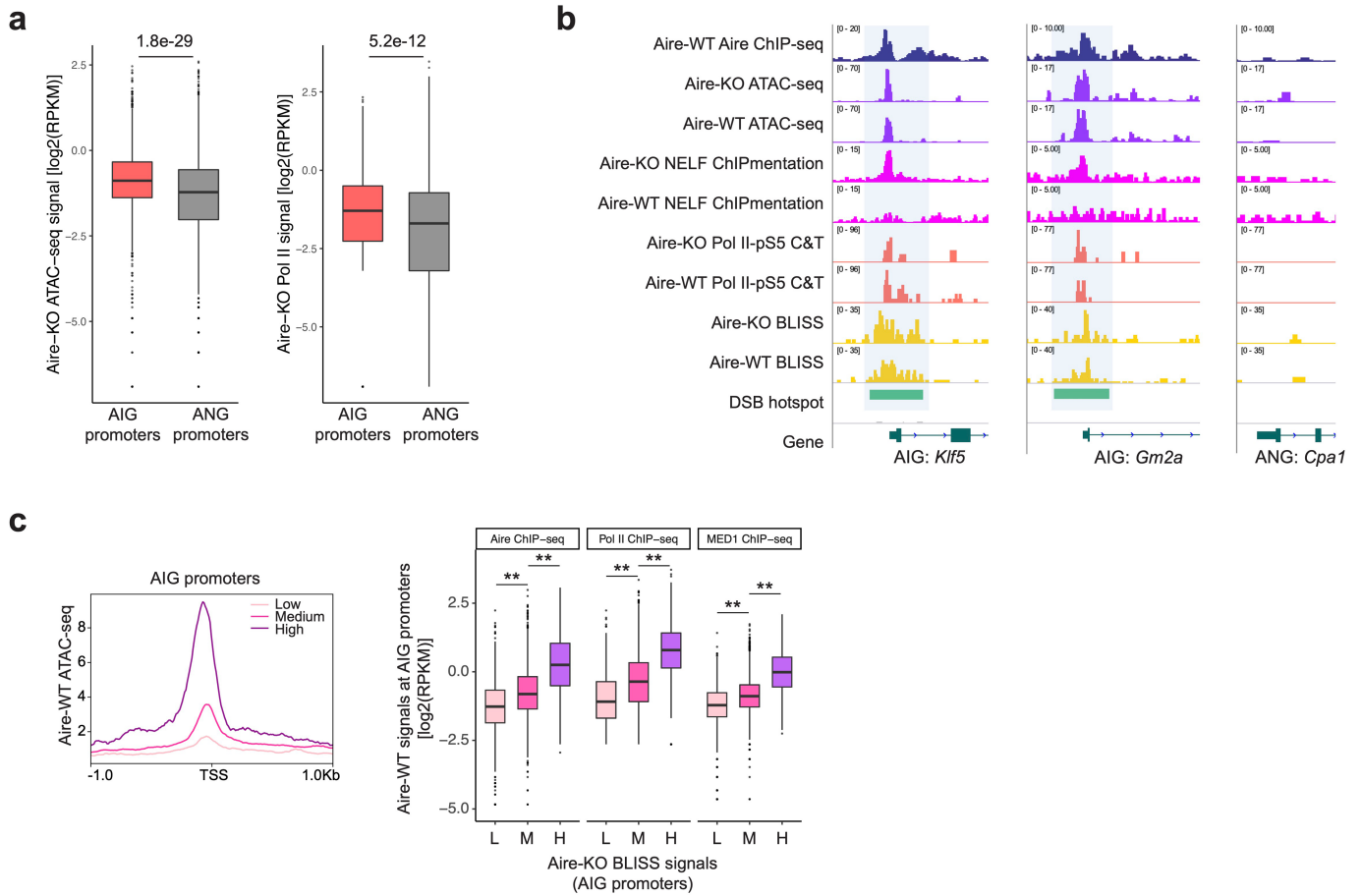
Extended Data Fig. 6 | Additional analysis of scRNA-seq of PBS-treated versus spermidine-treated mTECs, related to Fig. 3. a, Log2 ratio (M-values) versus log2 average (A-values) plots showing the effect of spermidine treatment on mTECs from wild-type mice. Red dots depict spermidine-specific AIRE-induced genes (FC > 2, p -value < 0.05). Dark grey dots depict AIRE-induced transcripts shared between mice injected with spermidine and PBS. **b**, Per-replicate UMAPs of scRNA-seq of mTEC^{hi} and post-AIRE mTEC^{lo} for PBS-treated

and spermidine-treated *Aire*-WT mice. Each dot on the UMAPs is a single cell ($n = 3184$). Each number on the UMAPs indicates a cluster identified using Seurat. **c**, Merged UMAPs of scRNA-seq of mTEC^{hi} and post-AIRE mTEC^{lo} from PBS-treated ($n = 2$ biological replicates) and spermidine-treated ($n = 2$ biological replicates) *Aire*-WT mice. mTEC subtypes were labeled. **d**, UMAPs showing the expression of *Aire* (left) and one MHC Class II gene (right).



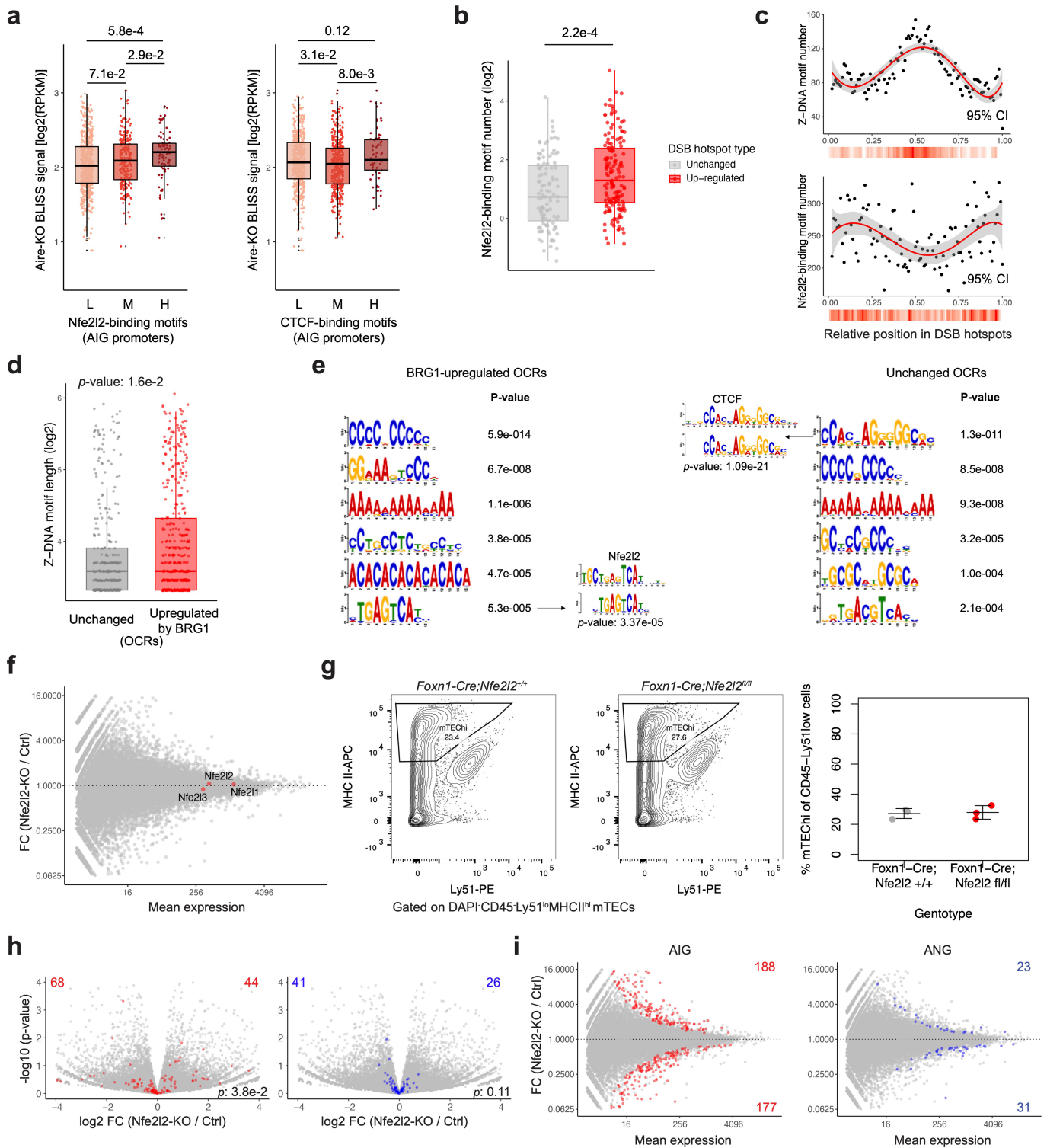
Extended Data Fig. 7 | Additional analysis of BLISS in mTECs, related to Fig. 4. **a**, Boxplot comparing BLISS signals at Z-DNA ChIP-seq peaks that had low, medium or high Z-DNA ChIP-seq signals in mTECs from *Aire*-WT mice. Low: <25th percentile (n = 1508); Medium: 25th - 75th percentile (n = 3008); High: > 75th percentile (n = 1506). **b**, Boxplot comparing *Aire*-KO BLISS signals at promoters of AIRE-inducible (n = 1563) and expression-matched AIRE-neutral genes in *Aire*-KO mTECs (n = 1907). AIRE-inducible and AIRE-neutral genes were weakly expressed genes (*Aire*-KO TPM < 0.35) whose promoter DSB generation was detected by BLISS in mTECs from *Aire*-KO mice. **c**, Boxplot comparing the enrichment of Z-DNA motifs (left) at DSB hotspots upregulated by spermidine

(n = 97) versus those unaffected by spermidine (n = 78). Analogous plot for CTCF-binding motifs is shown on the right. The number of motifs was normalized according to the length of the DSB hotspots. **d**, Correlation between genetic variation in CTCF-binding motifs and allelic imbalance in DSB generation. Individual lines indicate DSB hotspots with a stronger CTCF-binding motif match on the B6 allele (red, n = 60) or on the CAST allele (blue, n = 59). **e**, Analogous plot for (CA)_n repeats (n = 38 for B6 and n = 51 for CAST). *p*-values for panels **a-c** were calculated using the Wilcoxon rank sum test (two-tailed), and for panels **d** and **e** using the Kolmogorov-Smirnov (KS) test (two-tailed).



Extended Data Fig. 8 | Promoters of AIRE-induced genes were poised for expression prior to the engagement of AIRE. **a**, Boxplot comparing the ATAC-seq and Pol II ChIP-seq signals at promoters of AIRE-induced genes (n = 1563) versus those at expression-matched ANGs (n = 1907) in mTECs from *Aire*-KO mice. **b**, Exemplar DNA and chromatin profiles of AIRE-induced genes poised for expression in mTECs from *Aire*-KO mice. In comparison, exemplar

profiles for an ANG were shown on the right. **c**, Same as Fig. 4d except WT ATAC-seq and ChIP-seq signals. *p*-values in panels **a** and **c** were calculated using the Wilcoxon rank sum test (two-tailed). C&T: CUT&Tag; L: Low, n = 747; M: Medium, n = 2130; H: High, n = 322; *: *p*-value < 1e-10; **: *p*-value < 1e-20. Data for WT and *Aire*-KO ATAC-seq, WT Pol II and AIRE ChIP-seq came from ref. 9. Data for WT MED1 ChIP-seq came from ref. 94.

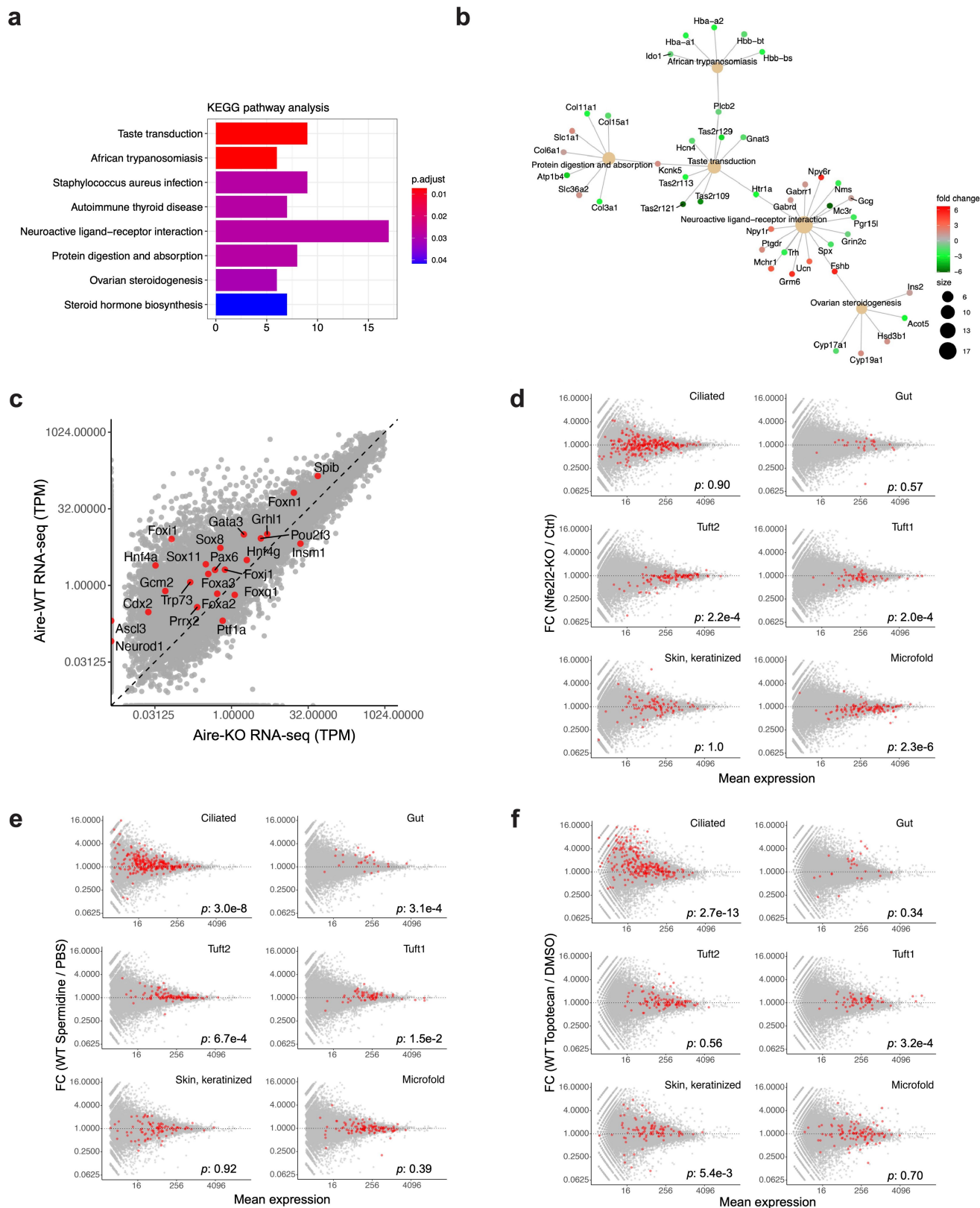


Extended Data Fig. 9 | See next page for caption.

Article

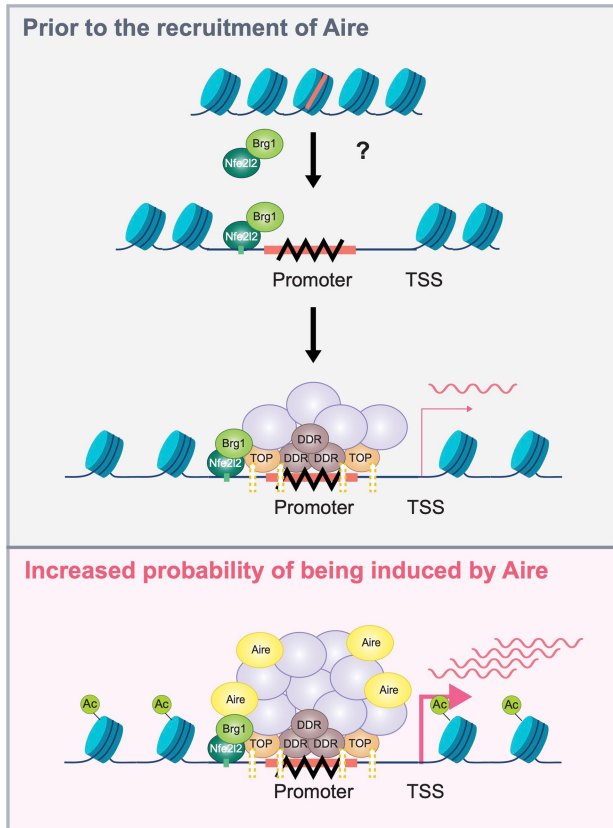
Extended Data Fig. 9 | NFE2L2 may cooperate with Z-DNA to poise AIRE-induced genes for expression. **a**, Boxplots comparing the *Aire*-KO BLISS signals at AIRE-induced gene promoter DSB hotspots containing varying numbers of NFE2L2-binding motifs (left) and CTCF-binding motifs (right). For NFE2L2-binding motifs: Low: ≤ 1 ($n = 598$); Medium: 2–5 ($n = 258$); High: > 5 ($n = 87$). For CTCF-binding motifs: Low: ≤ 1 ($n = 468$); Medium: 2–4 ($n = 404$); High: > 4 ($n = 71$). **b**, Boxplots comparing the enrichment of NFE2L2-binding motifs at DSB hotspots up-regulated by spermidine ($n = 159$) versus those unaffected by spermidine ($n = 104$). The number of motifs was normalized according to the length of the DSB hotspots. **c**, Density plots and heatmaps showing distributions of Z-DNA motifs (top) and NFE2L2-binding motifs (bottom) at DSB hotspots in promoters ($n = 6884$). Grey areas depict 95% confidence intervals. **d**, Boxplot comparing the lengths of Z-DNA motifs at OCRs

unchanged ($n = 282$) or up-regulated ($n = 356$) by BRG1 (See Methods) in mTECs. **e**, *De novo* motif analysis for OCRs unchanged versus up-regulated by BRG1. **f**, MA plot (log₂-scale) showing the expressions of NFE2-related factors in mTECs from *Nfe2l2*-KO and Ctrl mice. **g**, Representative cytofluorimetric plots and quantitative summary for mTECs from *Nfe2l2*-KO and Ctrl mice. Error bars, mean \pm s.e.m. from $n = 3$ biological replicates. **h**, Volcano plots showing the expression of AIRE-induced genes and ANGs that contain high-confidence NFE2L2-binding motifs at promoters in mTECs from *Nfe2l2*-KO and Ctrl mice. **i**, Differentially expressed AIRE-induced genes and ANGs (p -value < 0.05) between mTECs from *Nfe2l2*-KO and Ctrl mice. p -values for panels **a–b** and **d** were calculated using the Wilcoxon rank sum test (two-tailed), and for panel **h** using the Fisher's exact test (two-tailed). L: Low; M: Medium; H: High; CI: confidence interval. *Nfe2l2*-KO: *Foxn1*^{Cre}-*Nfe2l2*^{flox/flox}; Ctrl: control, *Foxn1*^{Cre}-*Nfe2l2*^{+/+}.



Extended Data Fig. 10 | Manipulation of Z-DNA formation, DSB generation or *Nfe2l2* expression affected the expression of signature genes of mTEC mimetic cells. a, KEGG pathway analysis (adjusted p -value < 0.05) for differentially expressed genes (p -value < 0.05, fold-change > 2, n = 745) between mTECs from *Nfe2l2*-KO and Ctrl mice. **b**, Network plot showing the significantly enriched downregulated KEGG pathways and the associated genes. **c**, Expression of lineage-defining TFs⁴² in WT versus *Aire*-KO AIRE-stage mTECs (log₂ scale). **d**, MA plots (log₂ scale) highlighting expression changes of

signature genes of several mimetic mTEC subtypes in mTECs from *Nfe2l2*-KO versus Ctrl mice. Red dots depict signature genes of the corresponding subtypes. **e-f**, Analogous plots showing the impact of spermidine and topotecan, respectively. Signature gene lists used were available at https://github.com/dmichelson/mimetic_cells/tree/main/scrna-seq/adult-neonate/mimetic-cell-signatures. p -values for panels **d-f** were calculated using the Fisher's exact test (two-tailed).



- H3K27ac
- DNA damage response proteins
- Topoisomerases
- Chromatin remodeler/Transcriptional machinery
- Nfe2l2 binding motif
- Z-DNA motif
- Z-DNA
- DNA double-stranded break
- mRNA
- Open chromatin
- Closed chromatin

Extended Data Fig. 11 | A model of Z-DNA's influence on AIRE target choice. Independent of AIRE, Z-DNA formation is more likely to occur at the promoters of genes having Z-DNA motifs but not under robust TF-mediated transcriptional control. NFE2L2 and other unknown factors would engage BRG1 or other

chromatin remodelers to stabilize the energetically unfavorable Z-DNA formation. Z-DNA would enhance DSB generation at the promoters of genes subject to AIRE induction, which would facilitate their poisoning, thereby promoting the recruitment of and induction of gene expression by AIRE.

Reporting Summary

Nature Portfolio wishes to improve the reproducibility of the work that we publish. This form provides structure for consistency and transparency in reporting. For further information on Nature Portfolio policies, see our [Editorial Policies](#) and the [Editorial Policy Checklist](#).

Statistics

For all statistical analyses, confirm that the following items are present in the figure legend, table legend, main text, or Methods section.

n/a Confirmed

- The exact sample size (n) for each experimental group/condition, given as a discrete number and unit of measurement
- A statement on whether measurements were taken from distinct samples or whether the same sample was measured repeatedly
- The statistical test(s) used AND whether they are one- or two-sided
Only common tests should be described solely by name; describe more complex techniques in the Methods section.
- A description of all covariates tested
- A description of any assumptions or corrections, such as tests of normality and adjustment for multiple comparisons
- A full description of the statistical parameters including central tendency (e.g. means) or other basic estimates (e.g. regression coefficient) AND variation (e.g. standard deviation) or associated estimates of uncertainty (e.g. confidence intervals)
- For null hypothesis testing, the test statistic (e.g. F , t , r) with confidence intervals, effect sizes, degrees of freedom and P value noted
Give P values as exact values whenever suitable.
- For Bayesian analysis, information on the choice of priors and Markov chain Monte Carlo settings
- For hierarchical and complex designs, identification of the appropriate level for tests and full reporting of outcomes
- Estimates of effect sizes (e.g. Cohen's d , Pearson's r), indicating how they were calculated

Our web collection on [statistics for biologists](#) contains articles on many of the points above.

Software and code

Policy information about [availability of computer code](#)

Data collection

Fastq data quality check: fastqc (v0.10.1, <https://www.bioinformatics.babraham.ac.uk/projects/fastqc/>).
Low-quality sequencing reads filtering and removal: Sickle (v1.33, <https://github.com/najoshi/sickle>).
Cell sorting: FACSARIA sorter (BD).

Data analysis

The pre-trained CNN model was implemented in TensorFlow (v1.14.0, <https://www.tensorflow.org/install>) and trained on 2 Tesla V100 GPU cards. The full model architecture with custom Python code is available at the following URL: <https://doi.org/10.5281/zenodo.10472904>
The fine-tuned model was implemented in TensorFlow (v2.3.0) and trained on 1 Tesla V100 GPU cards. The following software in Python (v3.6.11, <https://www.python.org/downloads/>) was used to interpret and visualize what the CNN model learned: pandas (v1.1.0), numpy (1.18.5), scipy (1.4.1), seaborn (v0.11.2), matplotlib (v3.3.0), MEME suite (v5.4.1, <https://meme-suite.org/meme/index.html>).
The RStudio (v1.4.463, <https://www.rstudio.com/categories/rstudio-ide/>) and custom R code (v3.5.1, <https://www.r-project.org/>) was used for statistical analyses, scatterplots, boxplots, MA plots and bar plots.
For non-F1-hybrid RNA-seq, RNA-seq reads were aligned using STAR (v2.7.3a, <https://github.com/alexdobin/STAR>). Differential expression analyses were performed using DESeq2 (v1.22.2, <https://bioconductor.org/packages/release/bioc/html/DESeq2.html>). For F1-hybrid RNA-seq, RNA-seq reads were aligned to the corresponding reference or alternative genome using Tophat2 (v2.1.1, <http://ccb.jhu.edu/software/tophat/tutorial.shtml>).
Sequencing reads of ATAC-seq, ChIP-seq, ChIPmentation, CUT&Tag and BLISS were aligned using bowtie2 (v2.3.4.3, <https://bowtie-bio.sourceforge.net/bowtie2/index.shtml>).
Post-processing of sequencing reads was performed using Samtools (v1.3.1, <https://www.htslib.org/download/>) and Picard (v2.8.0, <https://broadinstitute.github.io/picard/>).
Sequencing tracks were generated using deepTools (v3.0.2, <https://deeptools.readthedocs.io/en/develop/>), and displayed by Integrative Genomics Viewer (IGV, v2.5.0, <https://software.broadinstitute.org/software/igv/download>).

Sequencing profiles over various genomic regions (e.g. TSS) were generated using deepTools or the ngs.plot (v2.47.1, <https://github.com/shenlab-sinai/ngsplot>).
 ATAC-seq peaks and ChIP-seq peaks were identified using MACS2 (v2.1.1.20160309, <https://github.com/macs3-project/MACS/wiki/Install-macs2>).
 DNA double-strand breaks were called based on BLISS data using HOMER (v4.9, <http://homer.ucsd.edu/homer/index.html>) or MACS2 (v2.1.1.20160309, <https://github.com/macs3-project/MACS/wiki/Install-macs2>).
 Motif enrichment analyses were conducted using MEME suite (v5.4.1, <https://meme-suite.org/meme/index.html>).
 The KEGG pathway analysis for differentially expressed genes were performed using clusterProfiler (v3.10.1, <https://bioconductor.org/packages/release/bioc/html/clusterProfiler.html>).
 Flow cytometry analysis was performed using FlowJo (v10.8.1, <https://www.flowjo.com/solutions/flowjo>).

For manuscripts utilizing custom algorithms or software that are central to the research but not yet described in published literature, software must be made available to editors and reviewers. We strongly encourage code deposition in a community repository (e.g. GitHub). See the Nature Portfolio [guidelines for submitting code & software](#) for further information.

Data

Policy information about [availability of data](#)

All manuscripts must include a [data availability statement](#). This statement should provide the following information, where applicable:

- Accession codes, unique identifiers, or web links for publicly available datasets
- A description of any restrictions on data availability
- For clinical datasets or third party data, please ensure that the statement adheres to our [policy](#)

Basenji2 training, validation and test data were obtained from https://console.cloud.google.com/storage/browser/basenji_barnyard/data/mouse. All the sequencing data reported in this article were deposited as a SuperSeries at Gene Expression Omnibus (GEO) under accession GSE224557 (<https://www.ncbi.nlm.nih.gov/geo/query/acc.cgi?acc=GSE224557>). Specifically, the ATAC-seq, BLISS, ChIP-seq, ChIPmentation, CUT&Tag and bulk RNA-seq data are under accessions GSE224551, GSE224552, GSE224553, GSE224554, GSE224555 and GSE224556, respectively. Public datasets used in this article are: ATAC-seq for WT and Aire-KO mTECs from GSE92594; RNA Pol II, Aire and IgG ChIP-seq for WT mTECs from GSE92597; MED1 and IgG ChIP-seq for WT mTECs from GSE180937; ATAC-seq for mTECs from Brg1-WT and Brg1-cKO mice from GSE102526.

Human research participants

Policy information about [studies involving human research participants and Sex and Gender in Research](#).

Reporting on sex and gender

Use the terms sex (biological attribute) and gender (shaped by social and cultural circumstances) carefully in order to avoid confusing both terms. Indicate if findings apply to only one sex or gender; describe whether sex and gender were considered in study design whether sex and/or gender was determined based on self-reporting or assigned and methods used. Provide in the source data disaggregated sex and gender data where this information has been collected, and consent has been obtained for sharing of individual-level data; provide overall numbers in this Reporting Summary. Please state if this information has not been collected. Report sex- and gender-based analyses where performed, justify reasons for lack of sex- and gender-based analysis.

Population characteristics

Describe the covariate-relevant population characteristics of the human research participants (e.g. age, genotypic information, past and current diagnosis and treatment categories). If you filled out the behavioural & social sciences study design questions and have nothing to add here, write "See above."

Recruitment

Describe how participants were recruited. Outline any potential self-selection bias or other biases that may be present and how these are likely to impact results.

Ethics oversight

Identify the organization(s) that approved the study protocol.

Note that full information on the approval of the study protocol must also be provided in the manuscript.

Field-specific reporting

Please select the one below that is the best fit for your research. If you are not sure, read the appropriate sections before making your selection.

Life sciences Behavioural & social sciences Ecological, evolutionary & environmental sciences

For a reference copy of the document with all sections, see nature.com/documents/nr-reporting-summary-flat.pdf

Life sciences study design

All studies must disclose on these points even when the disclosure is negative.

Sample size

Sample sizes for sequencing replicates were two or three which are commonly used.
 The sample sizes for statistical tests were not predetermined.

Data exclusions	No data were excluded from analyses.
Replication	All of the sequencing experiments have two or three biological replicates with high correlation as detailed in the supplementary table.
Randomization	Mice under different ip injections were randomly allocated into experimental and control groups.
Blinding	Blinding was not relevant to this study because all the results were obtained based on objective quantitative analyses.

Reporting for specific materials, systems and methods

We require information from authors about some types of materials, experimental systems and methods used in many studies. Here, indicate whether each material, system or method listed is relevant to your study. If you are not sure if a list item applies to your research, read the appropriate section before selecting a response.

Materials & experimental systems

Methods

n/a	Involvement	n/a	Involvement
<input type="checkbox"/>	<input checked="" type="checkbox"/> Antibodies	<input type="checkbox"/>	<input checked="" type="checkbox"/> ChIP-seq
<input checked="" type="checkbox"/>	<input type="checkbox"/> Eukaryotic cell lines	<input type="checkbox"/>	<input checked="" type="checkbox"/> Flow cytometry
<input checked="" type="checkbox"/>	<input type="checkbox"/> Palaeontology and archaeology	<input checked="" type="checkbox"/>	<input type="checkbox"/> MRI-based neuroimaging
<input type="checkbox"/>	<input checked="" type="checkbox"/> Animals and other organisms		
<input checked="" type="checkbox"/>	<input type="checkbox"/> Clinical data		
<input checked="" type="checkbox"/>	<input type="checkbox"/> Dual use research of concern		

Antibodies

Antibodies used

For flow cytometric analysis and cell sorting: anti-MHCII-APC (107614, BioLegend), anti-Ly51-PE (108308, BioLegend), anti-CD45-PE/Cy7 (103114, BioLegend), anti-MHCII-PE (205308, BioLegend), anti-Ly51-Alexa Fluor 647 (108312, BioLegend), anti-CD4-Brilliant Violet 605 (100548, BioLegend), anti-CD8a-FITC (100706, BioLegend), anti-CD19-APC (115512, BioLegend), anti-Z DNA (ab2079, abcam).
For ChIPmentation, ChIP-seq and CUT&Tag: anti-Aire (14-5934-82, eBioscience), anti-NELF (ab170104, abcam), anti-rabbit IgG (611-201-122, Rockland), anti-RNA polymerase II phospho S5 (ab5131, abcam), anti-RNA polymerase II (MMS-128P, Covance), anti-Z-DNA/Z-RNA (Z22) (Ab00783-23.0, Absolute Antibody), Rabbit IgG (#2729, Cell Signaling)

Validation

Validation of the commercial antibodies were done by the manufacturers.
Below shows the relevant citations listed on the suppliers' websites for antibodies used in this article.

- anti-MHCII-APC (107614, BioLegend): <https://pubmed.ncbi.nlm.nih.gov/33177715/>
- anti-Ly51-PE (108308, BioLegend): <https://pubmed.ncbi.nlm.nih.gov/32338592/>
- anti-CD45-PE/Cy7 (103114, BioLegend): <https://pubmed.ncbi.nlm.nih.gov/33106654/>
- anti-MHCII-PE (205308, BioLegend): <https://pubmed.ncbi.nlm.nih.gov/33893298/>
- anti-Ly51-Alexa Fluor 647 (108312, BioLegend): <https://pubmed.ncbi.nlm.nih.gov/35042581/>
- anti-CD4-Brilliant Violet 605 (100548, BioLegend): <https://pubmed.ncbi.nlm.nih.gov/31079916/>
- anti-CD8a-FITC (100706, BioLegend): <https://pubmed.ncbi.nlm.nih.gov/31442407/>
- anti-CD19-APC (115512, BioLegend): <https://pubmed.ncbi.nlm.nih.gov/34788598/>
- anti-Z DNA (ab2079, abcam): <https://pubmed.ncbi.nlm.nih.gov/34735796/>
- anti-Aire (14-5934-82, eBioscience): <https://pubmed.ncbi.nlm.nih.gov/28135252/>
- anti-NELF (ab170104, abcam): <https://pubmed.ncbi.nlm.nih.gov/32102997/>
- anti-rabbit IgG (611-201-122, Rockland): <https://pubmed.ncbi.nlm.nih.gov/34901015/>
- anti-RNA polymerase II phospho S5 (ab5131, abcam): <https://pubmed.ncbi.nlm.nih.gov/33526923/>
- anti-RNA polymerase II (MMS-128P, Covance): <https://pubmed.ncbi.nlm.nih.gov/33453168/>
- anti-Z-DNA/Z-RNA (Z22) (Ab00783-23.0, Absolute Antibody): <https://pubmed.ncbi.nlm.nih.gov/35614224/>
- Rabbit IgG (#2729, Cell Signaling): <https://pubmed.ncbi.nlm.nih.gov/37744380/>

Animals and other research organisms

Policy information about [studies involving animals](#); [ARRIVE guidelines](#) recommended for reporting animal research, and [Sex and Gender in Research](#)

Laboratory animals

The mice used in this study were all 4-6-week-old females from the following backgrounds: homozygous C57BL/6J (B6), CAST/EiJ (CAST) and NOD/ShiLtJ (NOD); F1-hybrid: B6/NOD and B6/CAST.

Wild animals

This study did not involve wild animals.

Reporting on sex

All the mice used were females because previous studies on Aire were performed using female mice. To enable comparison with published data on Aire, we used female mice for this study.

Field-collected samples

Ethics oversight

Note that full information on the approval of the study protocol must also be provided in the manuscript.

ChIP-seq

Data deposition

- Confirm that both raw and final processed data have been deposited in a public database such as [GEO](#).
- Confirm that you have deposited or provided access to graph files (e.g. BED files) for the called peaks.

Data access links
May remain private before publication.

Files in database submission

Genome browser session (e.g. [UCSC](#))

Methodology

Replicates

Sequencing depth

Antibodies

Peak calling parameters

Data quality

Software

Plots

Confirm that:

- The axis labels state the marker and fluorochrome used (e.g. CD4-FITC).
- The axis scales are clearly visible. Include numbers along axes only for bottom left plot of group (a 'group' is an analysis of identical markers).
- All plots are contour plots with outliers or pseudocolor plots.
- A numerical value for number of cells or percentage (with statistics) is provided.

Methodology

Sample preparation

For cell sorting and flow cytometric analysis:

Thymus tissues from individual female mice were collected in Dulbecco's Modified Eagle Medium (DMEM; Gibco) supplemented with 2% fetal bovine serum (FBS) and 25mM HEPES (basic medium), and minced with scissors. The fragments were then digested for 20 min with 0.5mg/ml collagenase (Sigma-Aldrich) and 0.2mg/mL DNase (Sigma-Aldrich), then with collagenase/dispase (Roche) and 0.2mg/mL DNase (Sigma-Aldrich) for 15 min. CD45+ cells were depleted by magnetic-activated cell sorting (MACS) with CD45 MicroBeads (Miltenyi). For mice on B6 and B6/CAST background, cells were stained with the following primary antibodies: MHCII-APC (107614, BioLegend), Ly51-PE (108308, BioLegend); CD45-PE/Cy7 (103114, BioLegend). For mice on NOD and B6/NOD background, cells were stained with: MHCII-PE (205308, BioLegend), Ly51-Alexa Fluor 647 (108312, BioLegend); CD45-PE/Cy7 (103114, BioLegend). Cells were stained in the basic medium. 4',6-diamino-2-phenylindole (DAPI) was added before sorting to exclude dead cells. For flow cytometric analysis of thymocytes, the following primary antibodies were used: CD4-Brilliant Violet 605 (100548, BioLegend), CD8a-FITC (100706, BioLegend), CD19-APC (115512, BioLegend). For flow cytometric analysis of Z-DNA formation in mTECs, the anti-Z DNA antibody (ab2079, abcam) was used.

Instrument

FACSAria sorter (BD Biosciences) equipped with 4 lasers (355 (UV), 405, 488, and 638 nm) and 16 detector.

Software

Flow cytometry analysis was performed using FlowJo (v10.8.1, <https://www.flowjo.com/solutions/flowjo>).

Cell population abundance

Cell population abundances were determined using FlowJo (v10.8.1).

Gating strategy

FSC-A and SSC-A were used to exclude debris. Doublets were excluded using FSC-A and FSC-H gates. Live/dead staining by DAPI was used to get rid of dead cells. For F1-hybrid sequencing experiments, DAPI-,CD45-,Ly51lo,MHCIIhi,GFP^{hi} mTECs from B6 homozygous, NOD homozygous or B6/NOD F1 mice were sorted. For all other experiments, DAPI-,CD45-,Ly51lo,MHCIIhi mTECs were sorted.

- Tick this box to confirm that a figure exemplifying the gating strategy is provided in the Supplementary Information.